

# Sensitivity and information content of aerosol retrievals from the Advanced Very High Resolution Radiometer: radiometric factors

Alexander Ignatov

The sensitivity of aerosol optical depths  $\tau_1$  and  $\tau_2$  derived from the Advanced Very High Resolution Radiometer (AVHRR) channels 1 and 2, centered at  $\lambda_1 = 0.63$  and  $\lambda_2 = 0.83$   $\mu\text{m}$ , respectively, and of an effective Ångström exponent  $\alpha$ , derived therefrom as  $\alpha = -\ln(\tau_1/\tau_2)/\ln(\lambda_1/\lambda_2)$ , to calibration uncertainties, radiometric noise, and digitization is estimated. Analyses are made both empirically (by introduction of perturbations into the measured radiances and estimation of the respective partial derivatives) and theoretically (by use of a decoupled form of the single-scattering approximation of the radiative transfer equation). The two results are in close agreement. The errors,  $\Delta\tau_i$  and  $\Delta\alpha_i$ , are parameterized empirically as functions of  $\tau_i$ , radiometric errors, and Sun and view geometry. In particular, the  $\alpha$  errors change in approximately inverse proportion to  $\tau$  and are comparable with, or even exceed, typical  $\alpha$  signals over oceans when  $\tau < 0.25$ . Their detrimental effect on the information content of the AVHRR-derived size parameter gradually weakens as  $\tau$  increases. © 2002 Optical Society of America

OCIS codes: 010.1110, 010.1310, 120.5630, 120.0280, 280.1100, 280.1310.

## 1. Introduction

Stowe *et al.*<sup>1</sup> and Ignatov and Stowe<sup>2</sup> described an aerosol retrieval algorithm [termed internally in the National Environmental Satellite Data and Information Service (NESDIS) the second-generation algorithm] of the Advanced Very High Resolution Radiometer (AVHRR) onboard the National Oceanic and Atmospheric Administration (NOAA) polar orbiting satellites. The algorithm first derives two values of aerosol optical depths (AODs),  $\tau_1$  and  $\tau_2$ , at the monochromatic wavelengths  $\lambda_1 = 0.63$  and  $\lambda_2 = 0.83$   $\mu\text{m}$ , respectively, from individual reflectances in AVHRR channels 1 and 2, with two independent lookup tables. An effective Ångström exponent is then derived therefrom as

$$\alpha = -\frac{\ln(\tau_1/\tau_2)}{\ln(\lambda_1/\lambda_2)} \equiv \Lambda \ln \frac{\tau_1}{\tau_2}, \quad \Lambda \equiv -\frac{1}{\ln(\lambda_1/\lambda_2)}, \quad (1)$$

A. Ignatov (alex.ignatov@noaa.gov) is with the National Oceanic and Atmospheric Administration/National Environmental Satellite Data and Information Service, Office of Research and Applications, Division of Climate Research and Applications, Washington, D.C. 20233.

Received 12 March 2001; revised manuscript received 3 October 2001.

0003-6935/02/060991-21\$15.00/0

© 2002 Optical Society of America

where  $\Lambda$  is the spectral separation factor between the channels. For the AVHRR,  $\Lambda \approx 3.63$ .

The retrieval algorithm and its implementation with the 6S radiative transfer model<sup>3</sup> were documented by Ignatov and Stowe,<sup>2</sup> who used four NOAA-14 AVHRR data sets that were collected in the 5°–25°S global latitudinal belt in February 1998 ( $n = 67,092$  retrievals), April 1998 ( $n = 79,269$ ), January 1999 ( $n = 101,081$ ), and May 1999 ( $n = 108,286$ ). We use the same data here to estimate empirically the sensitivity of the retrieved  $\tau_i$  and  $\alpha$  to the AVHRR radiometric uncertainties.

AVHRR radiometric factors are subdivided into the categories of calibration, stability, radiometric noise, and digitization (the C, S, N, and D factors, respectively). Uncertainty in aerosol retrieval is quantitatively estimated as a response (partial derivative) to a perturbation, added to the real AVHRR measurement. Theoretical analysis is also possible, in which the reference data set of the top-of-the-atmosphere radiances (to which the perturbations are added, and about which partial derivatives are estimated) is simulated with a radiative transfer code at a number of Sun-view geometries and aerosol concentrations and types. There is no easy way, however, to define the multidimensional frequency distributions of geometrical and aerosol parameters that will be representative of the real retrieval conditions (to which the results of the sensitivity study are intended to be

applied). Note that the use of a real AVHRR as a reference implies that the reference data are already in error (contaminated by noise, digitized, and subject to calibration errors). For estimating partial derivatives, these perturbations, however, are of little importance as long as they remain relatively small. Note that use of the real AVHRR data as a reference was begun by Mishchenko *et al.*,<sup>4</sup> who qualitatively checked the sensitivity of their AOD and size parameter retrievals against some factors that influence retrievals, including the uncertainty in AVHRR calibration.

Many aspects of the analyses presented here have been considered in, and to a certain extent inspired by, the pioneering papers of Gordon,<sup>5,6</sup> who considered the effect of radiometric factors on the Coastal Zone Color Scanner and Moderate-Resolution Imaging Spectroradiometer retrievals of water-leaving radiance and chlorophyll concentration, and on the Ångström exponent as an intermediate product of the atmospheric correction algorithm. The present study is primarily a more-detailed and quantitative sensitivity study of atmospheric rather than oceanic parameters, specifically, with the AVHRR-like instruments that are now widely used for the global assessment of aerosols.<sup>1,2,4,7–10</sup>

In Section 2, AVHRR radiometric terms are defined: calibration slopes  $S_i$ , zero counts  $C_{i0}$ , noise-equivalent counts and albedos,  $NE\Delta C_i$  and  $NE\Delta A_i$  ( $\equiv \sigma_{A_i}$ ), respectively, and digitization in channels  $i = 1, 2$  ( $DA_i$ , corresponding to  $DC_i = 1$ ).

In Section 3, empirical sensitivities of the retrieved  $\tau_i$  and  $\alpha$  to the calibration slope uncertainties  $\varepsilon_{iC} = dS_i/S_i$  (or  $\varepsilon_{iC} = 100\% \times dS_i/S_i$  when error is expressed in percent rather than as a fraction), are documented. For these analyses, the radiances reported by the NOAA operations on the data sets are perturbed (multiplied) by  $(1 + \varepsilon_{iC})$ , and the respective deflections,  $\Delta\tau_{iC}$  and  $\Delta\alpha_{iC}$ , are calculated. It is shown that  $\Delta\tau_{iC} = (a_i + b_i\tau_i)\varepsilon_{iC}$ , where the coefficients  $a_i$  and  $b_i$  are channel specific. The perturbation in  $\alpha$ ,  $\Delta\alpha_{iC}$ , that is a result of perturbation in AOD in channel  $i$ ,  $\Delta\tau_{iC}$ , is approximated as  $\Delta\alpha_{iC} = \Lambda \ln(1 + \Delta\tau_{iC}/\tau_i)$ . For practical applications, the first term of the Taylor series,  $\ln(1 + \Delta\tau_{iC}/\tau_i) \approx \Delta\tau_{iC}/\tau_i$ , accurately approximates  $\Delta\alpha_{iC}$  as an inverse function of  $\tau_i$ . This result is consistent with the earlier analyses of Ignatov *et al.*<sup>11</sup> Neither  $\Delta\tau_{iC}$  nor  $\Delta\alpha_{iC}$  reveals Sun, view, scattering, and reflection geometry trends.

In Section 4 the effects of AVHRR radiometric noise ( $N$ ) and digitization ( $D$ ) on the retrievals of  $\tau_i$  and  $\alpha$  are empirically estimated with the same perturbation technique. The  $N$  and  $D$  signals differ by their probability-distribution functions only: The  $N$  signal is distributed normally, whereas the  $D$  signal is distributed uniformly. Otherwise, they influence the retrievals in a similar way, described by the same mathematics, and therefore their analyses have been combined in one section. In particular, both the  $N$  and the  $D$  signals introduce random errors in the retrievals (with standard deviations  $\sigma_{\tau iX}$  and  $\sigma_{\alpha iX}$ ,

respectively; here,  $X = N, D, ND$ ) but there is no bias. Separate analyses were performed for the  $N$  and  $D$  effects individually in channels 1 and 2, and the rules to estimate their combined effects are derived. The values of  $\sigma_{\tau iX}$  do not depend on  $\tau_i$ , whereas  $\sigma_{\alpha iX}$  change approximately in inverse proportion to  $\tau_i$ . Both  $\sigma_{\tau iX}$  and  $\sigma_{\alpha iX}$  show no trend with Sun angle, small trend with scattering angle, and significant trends with view and glint angles.

In Section 5 a simplistic analytical model of the AVHRR signals in channels 1 and 2 is formulated, based on a decoupled form of the single-scattering approximation for the radiative transfer equation, and used to derive analytical formulas for the sensitivities of the retrieved parameters to the radiometric uncertainties. This theoretical analysis provides an insight into the empirical AVHRR results obtained earlier in the paper and suggests how those results can be generalized for use with other sensor data.

In Section 6 the effects of the radiometric uncertainties on the information content of AVHRR aerosol measurements are discussed. A relative uncertainty is defined as the ratio of natural variability in  $\tau$  and  $\alpha$  to the  $C$ -,  $S$ -,  $N$ -, and  $D$ -induced errors in these parameters. It is shown that radiometric errors may substantially depreciate the AVHRR aerosol information content, and ways with which their corrupting effects on the retrievals can be partially alleviated are discussed.

In Section 7 the results are discussed and concluding remarks are made.

## 2. Radiometric Definitions for the AVHRR

### A. AVHRR Calibration Equation

AVHRR spectral radiances  $L_i$  [ $\text{W m}^{-2} \text{sr}^{-1} \mu\text{m}^{-1}$ ] are calculated as  $L_i = G_i^{-1}(C_i - C_{i0})$ . Here,  $G_i$  [counts/( $\text{W m}^{-2} \text{sr}^{-1} \mu\text{m}^{-1}$ )] is gain of channel  $i$  (see, e.g., Refs. 12–14),  $C_i$  is the measured count, and  $C_{i0}$  is the zero, or dark, count. According to Kidwell,<sup>15</sup> effective radiance measured in channel  $i$ ,  $N_i$  [ $\text{W m}^{-2} \text{sr}^{-1}$ ], is defined as  $N_i = L_i W_i$ , where  $W_i$  [ $\mu\text{m}$ ] is the equivalent width of the spectral channel, tabulated for several NOAA satellites by Kidwell.<sup>15</sup> For NOAA satellites up to and including NOAA-16, the equivalent widths lie in the ranges  $W_1 = 0.11$ – $0.14$  and  $W_2 = 0.22$ – $0.25 \mu\text{m}$ . In the NESDIS operations the effective radiances  $N_i$  are further converted to so-called overhead albedo units  $A_i$  by normalization to integrated solar spectral irradiance  $F_i$  [ $\text{W m}^{-2}$ ]:

$$A_i = \frac{\pi N_i}{F_i} \equiv \frac{\pi W_i L_i}{F_i} \equiv S_i(C_i - C_{i0}), \quad S_i \equiv \frac{\pi W_i}{G_i F_i}, \quad (2)$$

where  $S_i$  [counts<sup>-1</sup>] is the calibration slope. Occasionally, units of percent albedo are used, which are related to the fractional albedo defined by Eq. (2) as  $A_i(\%) = 100\% \times A_i$  (fractional). In this study the latter formulation is used.

Albedos defined by Eq. (2) are used as input to the aerosol retrieval algorithm after being corrected for

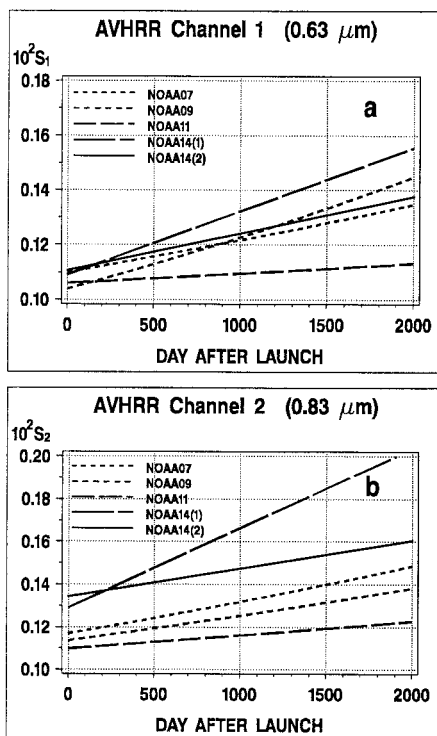


Fig. 1. Time series of calibration slopes of channels a, 1 and b, 2 for the AVHRR sensors on the NOAA satellites NOAA-07, NOAA-09, and NOAA-11, according to Rao and Chen<sup>22</sup>. For NOAA-14 the data are from (1) Rao and Chen<sup>14</sup> and (2) Rao.<sup>26</sup>

Sun–Earth distance. The uncertainty in albedo derived by Eq. (2) results from uncertainties in (1) the calibration slope,  $S_i$  (which results primarily from the uncertainty in gain,  $G_i$ , but may also be subject to the uncertainties in solar flux,  $F_i$ , and in the equivalent width of the spectral channel,  $W_i$ ) and in (2) the measured and dark (zero) counts,  $C_i$  and  $C_{i0}$ , that result from radiometric noise and digitization.

#### B. AVHRR Calibration Slope and Its Stability

The AVHRR calibration slope is not monitored in flight and is therefore determined vicariously. Extensive use of the AVHRR for quantitative applications that were not foreseen originally, such as measuring vegetation over land and aerosols over oceans, called for many efforts to calibrate the AVHRR after it was launched.<sup>14,16–26</sup> The problem is further complicated by the fact that the calibration slopes change dramatically not only from satellite to satellite but also over the life of a NOAA satellite.

Figure 1 plots values of  $S_1$  and  $S_2$  as a function of time for a few NOAA satellites. For NOAA-7, NOAA-9, and NOAA-11, the results of Rao and Chen<sup>22</sup> were used. For NOAA-14, two calibration curves are shown. The first<sup>14</sup> was used in NOAA operations before 8 December 1998 (in particular, with the February 1998 and April 1998 data). The second<sup>26</sup> was integrated into NOAA operations on 8 December 1998 (and was used with the January 1999 and May 1999 data; see Ref. 2 for details).

The example of the NOAA-14 satellite clearly dem-

onstrates the degree of uncertainty in calibration slopes  $S_i$ , even when a consistent calibration methodology is applied by the same authors but to a different time series of satellite data. The uncertainty may be even larger if different calibration methodologies are used by different investigators. For AVHRR channel 1, Mitchell *et al.*<sup>19</sup> estimated that the uncertainty of the calibration slope determinations by individual vicarious techniques is in the range  $\pm 3$ – $\pm 5\%$  and typically is within  $\pm 5\%$  when an ensemble of results is considered. Mitchell *et al.*<sup>19</sup> suggest that the uncertainty in channel 2 is larger, because the signal is generally lower in this channel (e.g., over the bright desert calibration targets). Furthermore, there is an additional variable factor that influences the satellite signal in this channel (strong water-vapor absorption). These estimates are in broad agreement with the results by a vast majority of other authors,<sup>13,14,20,22,24,25</sup> with an upper limit of uncertainty as reported by Che and Price<sup>12</sup> of  $\pm 10\%$ . Summarizing information from various authors and sources yields an uncertainty in the calibration slope of  $\pm 5\%$  in AVHRR channel 1 and of  $\pm 7\%$  in channel 2.

It should be emphasized that the estimates for the best-case situation described above represent the highest level of accuracy attainable at present time with the use of the best vicarious calibration techniques available. The uncertainties are unavoidably larger in the operational reality because the time series used in estimating the trends are shorter, because of the operational implementation pressure, and because extrapolation rather than interpolation must be used (as a result of the lack of temporal context on the time axis to the right of the retrieval point). For instance, for the four NOAA-14 data sets used in this study, the calibration slopes derived with the use of the two versions of calibrations, those of Rao and Chen<sup>14</sup> and of Rao,<sup>26</sup> differ by approximately 7–10% in channel 1 and by approximately 13–20% in channel 2 for the February 1998–May 1999 period. These numbers are illustrative of the real uncertainty of the calibration slope that one should expect to encounter in the AVHRR operational day-to-day reality.

Equation (2) suggests that there are other sources of potential errors in  $S_i$ . One is associated with the uncertainties in the solar flux,  $F_i$ , which is customarily calculated by use of the Neckel–Labs<sup>27</sup> data but that may be uncertain by a few percent in certain parts of the solar spectrum.<sup>6</sup> The other is the equivalent width of the spectral channel,  $W_i$ , calculated from channel's spectral response. The AVHRR's spectral filters are not controlled in flight, and a suspicion was raised that they may change over a satellite's lifetime.<sup>23</sup> Additionally, aerosol remote sensing is in the so-called low-signal regime. According to Mitchell,<sup>28</sup> "counts observed over dark ocean for clean maritime conditions are typically in the range  $20 < (C_1 - C_{10}) < 50$  (channel 1) and  $10 < (C_2 - C_{20}) < 30$  (channel 2)." The calibration methodology of Rao and Chen<sup>14,22,26</sup> uses bright desert targets for calibration. Although we know of no



analyses that have shown any hint of nonlinearity in the AVHRR response,<sup>29</sup> the sharp differences in the brightness of the calibration and retrieval targets may be an additional source of aerosol errors.

Summarizing, the best-case uncertainties in the calibration slopes, derived by a suite of several vicarious calibration techniques from sufficiently long time series after the satellite mission is completed, are estimated to be within  $\pm 5\%$  and  $\pm 7\%$  in AVHRR channels 1 and 2, respectively. In operational reality, the uncertainties may be larger by a factor of 2 or so, of the order of  $\pm 10\%$  and  $\pm 15\%$  in AVHRR channels 1 and 2, respectively. Below, errors to be expected in the operational aerosol retrievals, and in postoperation reprocessing such as in the Global Aerosol Climatology Project (GACP; Ref. 4) or the Pathfinder Atmosphere (PATMOS; Ref. 30) data set, are quantified.

Long-term trends and discontinuities in calibration, if present, are relevant to the stability of the calibration (the  $S$  errors). Stability error differs from calibration error in that it characterizes how well a vicarious technique, which assumes a stable external target and is therefore expected to provide a stable calibration record, allows one to achieve this objective. The artifacts in the calibration record, if present, are therefore indicative of the residual errors (imperfections) of the vicarious calibration techniques. These errors may result from a less-than-perfect separation of the calibration effect from angular variability in the AVHRR signal over the calibration target, from the type of fit (e.g., linear or exponential) used to approximate the degradation rate of a calibration parameter, and from the insufficient or incomplete seasonal cycle time series. Estimates of the stability of various AVHRR vicarious calibration techniques are usually well beyond the capability level of those techniques and are therefore not available from the literature. What is more, the numerical estimates below suggest that the sensitivity can be indirectly inferred from a time series of the derived aerosol parameters, which happen to be a sensitive indicator of any problem here and that one may therefore use to approach its analysis and correction.

#### C. Zero Count, $C_{i0}$

The zero count is controlled in flight, but historically a constant value of  $C_{i0}$  is used in the operations [for example, for NOAA-14,  $C_{10} = C_{20} = 41$  (Ref. 22)]. Mitchell<sup>28</sup> analyzed time series of  $C_{i0}$  from NOAA-9, NOAA-11, NOAA-12, and NOAA-14 to estimate specifically the long-term trends, excursions, and discontinuities in the mean  $C_{i0}$  and the noise in the zero count,  $NE\Delta C_{i0}$ .

##### 1. Trends and Discontinuities in the Zero Count

Mitchell<sup>28</sup> found that NOAA-12 channel 2 showed "significant but continuous excursions over the last year of its life," whereas NOAA-11 channel 1 "displayed notable discontinuities." Deviations in these cases were within a  $\Delta C_{i0}$  value of 0.3–0.5 counts.

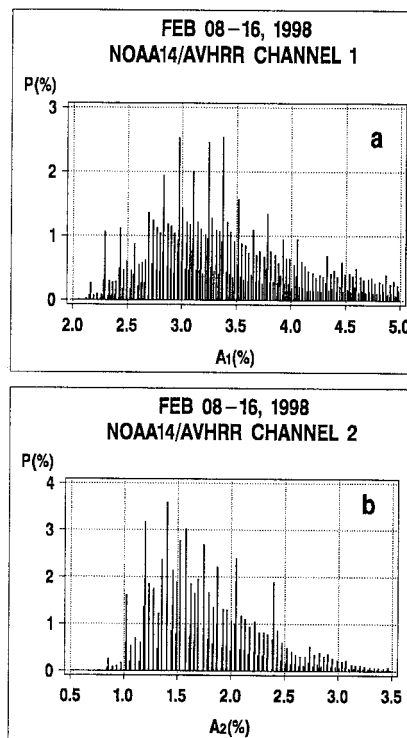


Fig. 2. Histograms of actual AEROS albedos in channels 1 and 2.

Mitchell<sup>28</sup> specifically emphasized that, in the low-radiance regime, these deviations are equivalent to calibration slope errors of  $\epsilon_{2C} \sim 1.6 \dots 4.0\%$  for NOAA-12 channel 2 and  $\epsilon_{1C} \sim 1 \dots 3\%$  for NOAA-11 channel 1. For NOAA-14, no notable time changes were observed; mean values of  $C_{10}$ ,  $C_{20}$  were within 40.9–41.0. Therefore the assumptions of constant  $C_{10}$  and  $C_{20}$  seem to hold for NOAA-14. (Note that Mitchell<sup>28</sup> analyzed only the first eight months of NOAA-14 operation, January–September 1995).

##### 2. Noise in Zero Count $NE\Delta C_{i0}$

Mitchell<sup>28</sup> estimated  $NE\Delta C_{i0}$  in flight and found that  $NE\Delta C_{10} \sim NE\Delta C_{20} \sim 0.20$  counts for all four satellites, NOAA-9, NOAA-11, NOAA-12, and NOAA-14. These in-flight estimates (which were typically 30–40% lower than the respective preflight measurements) were used for the numerical estimates below.

#### D. Radiometric Noise and Digitization

Figure 2 shows histograms of aerosol observation (AEROS) albedos. One should keep in mind that the AEROS data used in this study are modified global area coverage (GAC) data. Each AEROS data point represents an average radiometrically calibrated albedo of  $2 \times 2$  arrays of those GAC pixels, which are identified as cloud free by the operational Sea Surface Temperature/Aerosol cloud mask algorithm.<sup>31</sup> There may be one to four cloud-free GAC pixels within an array. Additionally, geography (latitude and longitude), observation geometry (Sun, view, and relative azimuth angles), brightness tem-

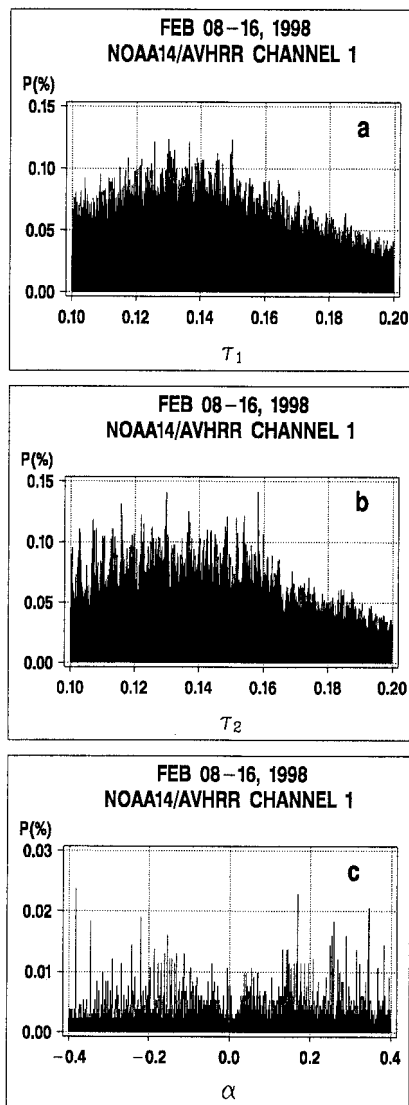


Fig. 3. Fragments of histograms of aerosol optical depth retrievals in channel 1: a, b, from AEROS albedos shown in Fig. 2 and c, the Ångström exponent derived therefrom.

peratures (in AVHRR channels 3–5), sea-surface temperatures, and aerosol optical depths are also stored in the AEROS files. The averaging over one to four cloud-free GAC pixels, along with noise and digitization in the data, superimposed upon the physical signal contributes to the complexity of the albedos in Fig. 2.

Figure 3 further illustrates the effect of radiometric noise and digitization on retrieved  $\tau_1$ ,  $\tau_2$ , and  $\alpha$ . The artifacts observed in the albedos are somewhat smoothed out by the variable Sun and view geometry used in the retrievals, but they are still clearly traced in the data.

### 1. Noise in Effective Count $C_{\text{eff}} \equiv (C - C_0)$

The measured count,  $C_i$ , is subject to the same radiometric noise as the zero count, i.e.,  $\text{NE}\Delta C_1 \sim \text{NE}\Delta C_2 \sim 0.20$ . Assuming that the noise in  $C_i$  is independent of that of  $C_{i0}$ , one obtains for the noise in

the effective count [defined as  $C_{\text{eff},i} = (C_i - C_{i0})$ ]  $(\text{NE}\Delta C_{\text{eff},i}) \sim 0.2 \times \sqrt{2} \sim 0.28$ . The AEROS data used in this study are expressed in albedo units. Therefore, for the perturbation analysis in Section 4 below, one needs noise expressed in albedo units,  $\text{NE}\Delta A_i \equiv \sigma_{A_i}$ , consistently with the data. Equation (2) suggests that  $\text{NE}\Delta A_i = S_i(\text{NE}\Delta C_{\text{eff},i})$ , and Fig. 1 and the analyses by Ignatov and Stowe<sup>2</sup> suggest that  $S_1 \sim 1.3 \times 10^{-3}$  and  $S_2 \sim 1.5 \times 10^{-3}$  for the February 1998–May 1999 period that is covered by the data. Substituting the latter into the former, one obtains  $\text{NE}\Delta A_1 \equiv \sigma_{A_1} \sim 3.6 \times 10^{-4}$  and  $\text{NE}\Delta A_2 \equiv \sigma_{A_2} \sim 4.2 \times 10^{-4}$ . These numbers are used for the numerical estimates in Section 4.

### 2. Digitization

Digitization in a channel,  $\text{DA}_i$ , is defined as an albedo response to a unit increment in the respective satellite count,  $\Delta C_i = 1$ . One obtains these responses by substituting  $\Delta C_i = 1$  into Eq. (2):  $\text{DA}_i = S_i$ , i.e.,  $\text{DA}_1 = S_1 \sim 1.3 \times 10^{-3}$  and  $\text{DA}_2 = S_2 \sim 1.5 \times 10^{-3}$ . These values are used for the numerical estimates in Section 4 below. Note that no digitization error is assumed in the zero count,  $C_{i0}$ .

### 3. Empirical Sensitivity of $\tau_i$ and $\alpha$ to the Uncertainty in Calibration Slope

A perturbation to the calibration slope,  $\Delta S_i$ , was introduced, and perturbations in AOD in the respective channel,  $\Delta \tau_{iC}$ , and the resultant Ångström exponent,  $\Delta \alpha_{iC}$ , were estimated. Note that, because of the specifics of the algorithm (i.e., independent  $\tau$  retrievals in the two channels), calibration in channel 1 influences retrievals only in channel 1 (and not in channel 2). Likewise, calibration in channel 2 influences retrievals only in channel 2 (and not in channel 1).

Four values of perturbation have been considered, i.e.,  $\epsilon_{iC} = \Delta S_i/S_i = +0.05, +0.10, +0.15, +0.20$  ( $+5\%, +10\%, +15\%, +20\%$  error, respectively, in the calibration slope). Eight numerical experiments were conducted (four in channel 1 and four in channel 2, separately). In this section the observed perturbations,  $\Delta \tau_{iC}$  and  $\Delta \alpha_{iC}$ , are related to  $\epsilon_{iC}$  and to retrieval conditions.

#### A. Aerosol Optical Depths

Figure 4 shows perturbations  $\Delta \tau_{1C}$  as a function of  $\tau_1$  on the left and  $\Delta \tau_{2C}$  as a function of  $\tau_2$  on the right for the four values of  $\epsilon_{iC}$  ( $=+0.05, +0.10, +0.15, +0.20$ , in rows) for the February 1998 data set. Remarkably consistently, the data, which represent a wide variety of geographical conditions and Sun-view, scattering, and reflection geometries, show a linear relationship between perturbation  $\Delta \tau_{iC}$  and  $\tau_i$ :

$$\Delta \tau_{iC} = a_i' + b_i' \times \tau_i. \quad (3)$$

The slope  $a_i'$  and the intercept  $b_i'$  of the relationship depend linearly on  $\epsilon_{iC}$ , as documented in Fig. 5:

$$a_i' = a_i \epsilon_{iC}, \quad b_i' = b_i \epsilon_{iC}. \quad (4)$$

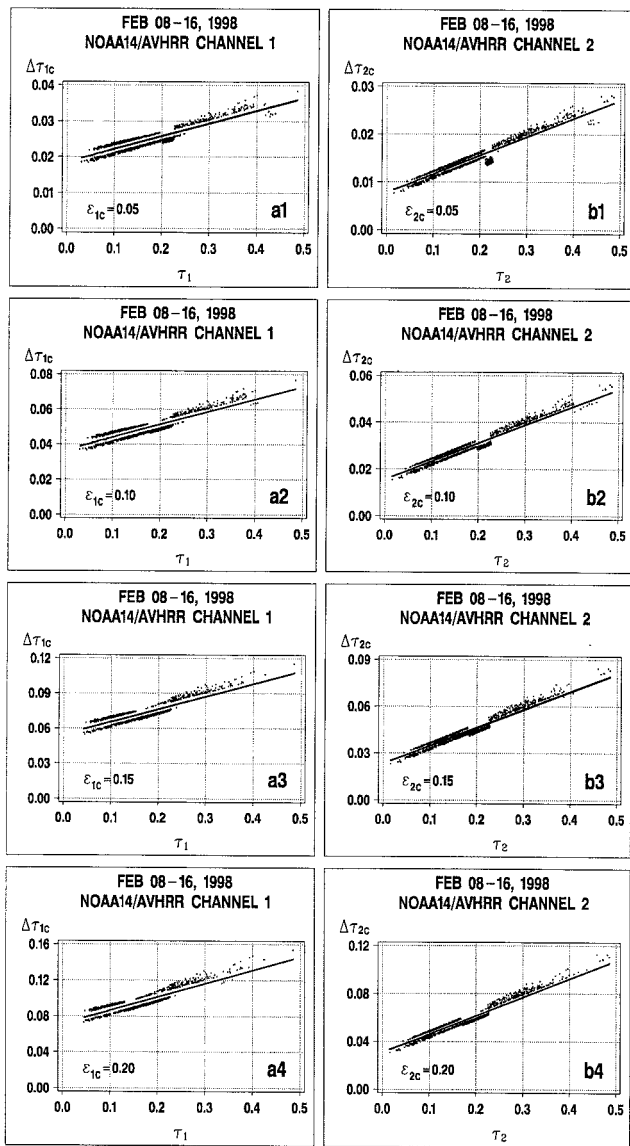


Fig. 4. Perturbations in aerosol optical depths  $\Delta\tau_{iC}$  versus  $\tau_i$  that result from perturbation in the calibration slopes  $\varepsilon_{iC} = \Delta S_i/S_i$  and linear fit according to Eqs. (5) in AVHRR channels 1 ( $i = 1$ ) and 2 ( $i = 2$ ) for four values of calibration error:  $\varepsilon_{iC} = 0.05, 0.10, 0.15, 0.20$ .

Figure 5 shows, and Table 1 lists, coefficients  $a_i$  and  $b_i$  for all four data sets used in this study. Using data from the rightmost column of Table 1, we can summarize the findings of this subsection as follows:

$$\Delta\tau_{1C} = [(0.370 \pm 0.011) + (0.714 \pm 0.023)\tau_1]\varepsilon_{1C}, \quad (5a)$$

$$\Delta\tau_{2C} = [(0.158 \pm 0.004) + (0.742 \pm 0.030)\tau_2]\varepsilon_{2C}, \quad (5b)$$

where  $\pm$  characterizes the variability of the regression parameters from one data set to the other, as derived from Table 1.

Note an important asymptote of Eqs. (5): the error in  $\tau_i$  vanishes ( $\Delta\tau_{iC} \rightarrow 0$ ) when the respective

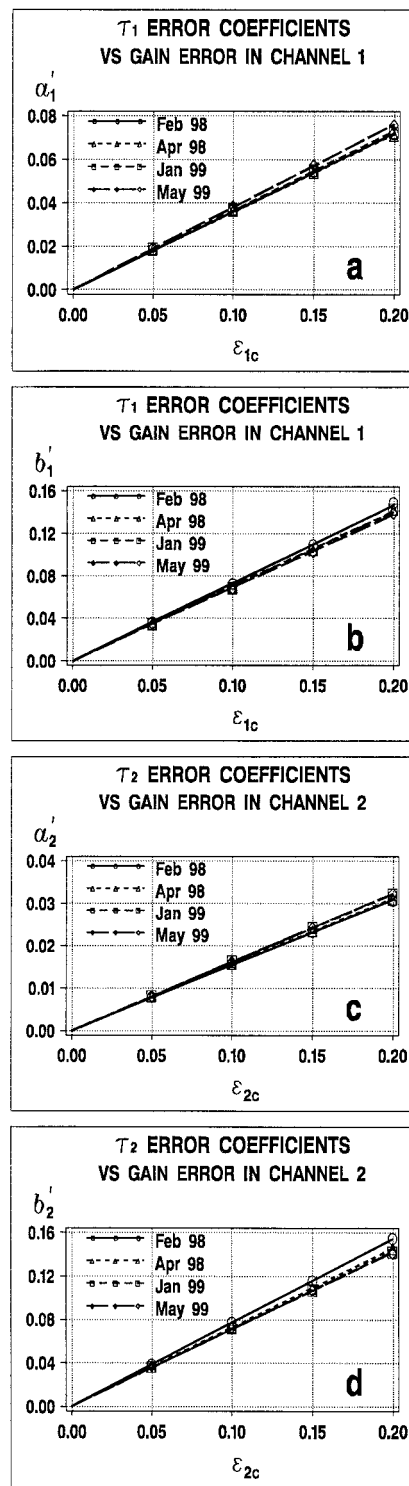


Fig. 5. Coefficients of linear Eq. (3): slope,  $a_i'$  and intercept  $b_i'$  in AVHRR channels 1 and 2 versus calibration slope perturbation,  $\varepsilon_{iC} = \Delta S_i/S_i$ , for the four data sets used in this study.

calibration error is small ( $\varepsilon_{iC} \rightarrow 0$ ). The error, however, does not vanish at low aerosol ( $\tau_i \rightarrow 0$ ) when calibration error is present but rather approaches  $\Delta\tau_{iC0} \rightarrow a_i\varepsilon_{iC}$ . Note that this component of error differs in the two channels (it is approximately 2.2–2.5 times higher in channel 1 than in channel 2). In

**Table 1. Coefficients of Eqs. (4) That Represent Aerosol Optical Depth Error**

Parameter: Method	Time of Data Collection				Summary
	February 1998	April 1998	January 1999	May 1999	
$\alpha_1$					
Empirical:	0.362	0.359	0.366	0.381	$0.370 \pm 0.011$
theory, Eqs. (14)	$0.49 \pm 0.05$	$0.52 \pm 0.08$	$0.52 \pm 0.08$	$0.54 \pm 0.06$	$0.52 \pm 0.08$
$\alpha_2$					
Empirical:	0.154	0.156	0.161	0.162	$0.158 \pm 0.004$
theory, Eqs. (14)	$0.175 \pm 0.015$	$0.180 \pm 0.020$	$0.175 \pm 0.020$	$0.185 \pm 0.015$	$0.180 \pm 0.020$
$b_1$					
Empirical:	0.737	0.703	0.706	0.691	$0.714 \pm 0.023$
theory, Eqs. (14)	1	1	1	1	1
$b_2$					
Empirical:	0.772	0.729	0.715	0.712	$0.742 \pm 0.030$
theory, Eqs. (14)	1	1	1	1	1

particular, for  $\varepsilon_{1C} = \varepsilon_{2C} = +0.10$  (a +10% error in calibration slopes) one obtains that  $\Delta\tau_{1C0} \sim 0.037$  and  $\Delta\tau_{2C0} \sim 0.016$ , even if aerosol is not present (i.e., if  $\tau_1 = \tau_2 = 0$ ).

The  $b_i$  parameters characterize the sensitivity of  $\Delta\tau_{iC}$  to  $\tau_i$ . Unlike the  $a_i$  parameters, the  $b_i$  parameters have similar values in the two channels:  $b_1 \approx b_2$ , well within their uncertainties. According to Eqs. (5), the estimates of  $\Delta\tau_{iC0}$  obtained at  $\tau_i = 0$  should be raised by  $\delta(\Delta\tau_{iC}) \sim 0.007$  for each increment in  $\delta\tau_i \sim 0.1$  in either channel.

The physical meanings of these parameters and relationships are discussed in Section 5 below.

#### B. Ångström Exponent

Figure 6 documents perturbations in the retrieved Ångström exponent,  $\Delta\alpha_{iC}$ , that result from the corresponding perturbations in the calibration slopes,  $\varepsilon_{iC}$ , in channels 1 (left) and 2 (right), for the four values of  $\varepsilon_{iC}$  ( $= +0.05, +0.10, +0.15, +0.20$ ) relative to  $\tau_1$  and  $\tau_2$ , respectively. Again, the full set of empirical observations collected under the wide variety of geographical and illumination, observation, scattering, and reflection geometry conditions forms a remarkably coherent pattern of progressively increasing error in the Ångström exponent as  $\tau$  decreases.

This result is better understood if one recalls that  $\Delta\alpha_{iC}$  are calculated with the use of Eq. (1) as

$$\begin{aligned} \Delta\alpha_{1C} &= \Lambda \left[ \ln \left( \frac{\tau_1 + \Delta\tau_{1C}}{\tau_2} \right) - \ln \left( \frac{\tau_1}{\tau_2} \right) \right] \\ &= +\Lambda \ln \left( 1 + \frac{\Delta\tau_{1C}}{\tau_1} \right), \end{aligned} \quad (6a)$$

$$\begin{aligned} \Delta\alpha_{2C} &= \Lambda \left[ \ln \left( \frac{\tau_1}{\tau_2 + \Delta\tau_{2C}} \right) - \ln \left( \frac{\tau_1}{\tau_2} \right) \right] \\ &= -\Lambda \ln \left( 1 + \frac{\Delta\tau_{2C}}{\tau_2} \right). \end{aligned} \quad (6b)$$

Figure 7 shows scattergrams of  $\Delta\alpha_{iC}$  versus  $\Delta\alpha_{iC, \text{est}}$ , where estimated values are obtained by sub-

stitution of the fit formulas for  $\Delta\tau_{iC}$  given by Eqs. (5) into Eqs. (6) in place of the actual value,  $\Delta\tau_{iC}$ :

$$\begin{aligned} \Delta\alpha_{1C} &= +\Lambda \\ &\ln \left[ 1 + \frac{(0.370 \pm 0.011) + (0.714 \pm 0.023)\tau_1}{\tau_1} \varepsilon_{1C} \right], \end{aligned} \quad (7a)$$

$$\begin{aligned} \Delta\alpha_{2C} &= -\Lambda \\ &\ln \left[ 1 + \frac{(0.158 \pm 0.004) + (0.742 \pm 0.030)\tau_2}{\tau_2} \varepsilon_{2C} \right]. \end{aligned} \quad (7b)$$

Figure 7 suggests that Eqs. (7) can be used not only for qualitative analysis of the effect of calibration on the derived Ångström exponent but also for the accurate numerical prediction of this effect.

Note that the error in the Ångström exponent, which results from simultaneous calibration errors in the two channels, is estimated as the arithmetic sum of the two components in Eqs. (7):  $\Delta\alpha_C = \Delta\alpha_{1C} + \Delta\alpha_{2C}$ , taken with their respective signs. Assuming for the sake of estimate that  $\tau_1 \sim \tau_2 \sim 0.15$  (which are representative, according to the analysis of Ignatov and Stowe,<sup>32</sup> of typical AODs for the four data sets used in this study),  $\varepsilon_{1C} \sim +0.05$ , and  $\varepsilon_{2C} \sim +0.07$  (a +5% calibration slope error in channel 1 and a +7% error in channel 2), one obtains  $\Delta\alpha_{1C} \sim +0.53$ ,  $\Delta\alpha_{2C} \sim -0.43$ , and  $\Delta\alpha_C = +0.53 - 0.43 = +0.10$ . In this example the signs of the Ångström exponent errors are counterdirected in the two channels; i.e., a positive calibration slope error,  $\varepsilon_{iC} > 0$ , results in a positive Ångström exponent error in channel 1 ( $\Delta\alpha_{1C} > 0$ ) but in a negative error in channel 2 ( $\Delta\alpha_{2C} < 0$ ). This is so because a positive calibration error,  $\varepsilon_{iC} > 0$ , always results in a positive AOD error,  $\Delta\tau_{iC}$ , one of which ( $\Delta\tau_{1C}$ ) appears in the numerator of the ratio given by Eq. (1) and the other of which ( $\Delta\tau_{2C}$ ) is found in the denominator. Note that the same calibration slope error in the channels,  $\varepsilon_{1C} = \varepsilon_{2C}$ , would have a bigger effect if it occurred in channel 1, especially at low  $\tau$ . This is so because the



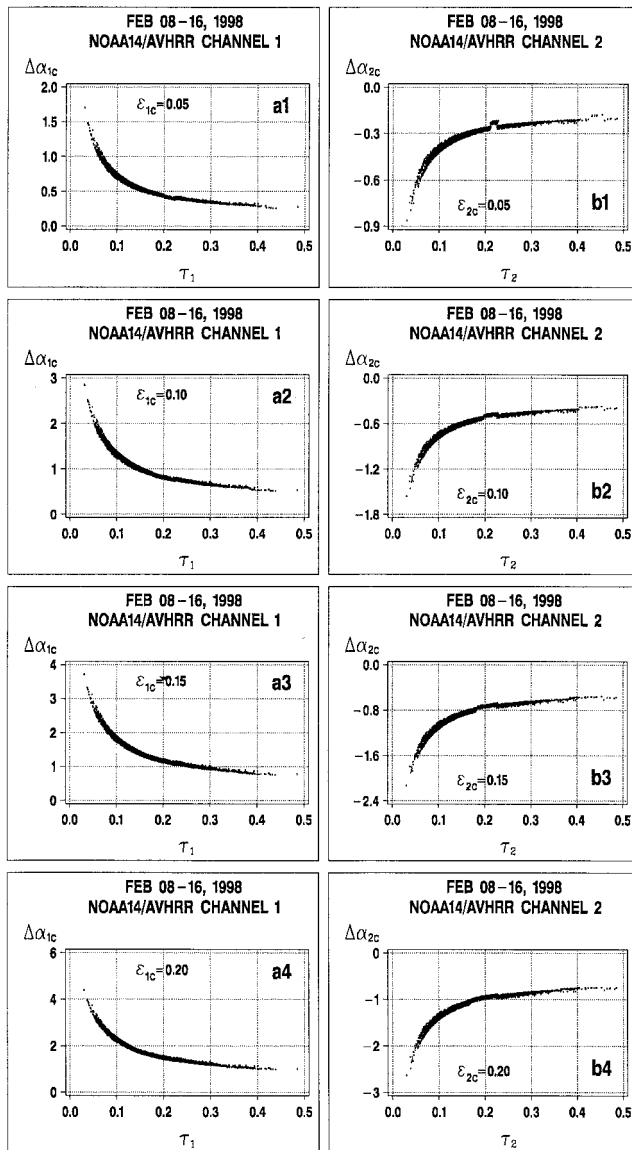


Fig. 6. Perturbations  $\Delta\alpha_i$  in the Ångström exponent resulting from perturbations in the calibration slopes  $\varepsilon_{iC} = \Delta S_i/S_i$  in AVHRR channels 1 ( $i = 1$ ) and 2 ( $i = 2$ ) for four values of calibration error:  $\varepsilon_{iC} = 0.05, 0.10, 0.15, (3) 0.05$ .

calibration-induced  $\tau$  error in channel 1 is approximately 2.2–2.5 times larger than in channel 2 ( $\Delta\tau_{1C} > \Delta\tau_{2C}$ ), whereas the ratio of  $\tau_1/\tau_2$  never exceeds  $\sim 1.74$  (when  $\alpha = 2$ ).

A few asymptotes of Eqs. (7) are particularly important. If the calibration error is small ( $\varepsilon_{iC} \rightarrow 0$ ), the respective error  $\tau$  will vanish ( $\Delta\tau_{iC} \rightarrow 0$ ), as discussed above, and so generally will the error in  $\alpha$ , with the exception of the case of low  $\tau$ . Equations (7) suggest that, when  $\tau_i \rightarrow 0$ , then  $\Delta\alpha_{iC} \rightarrow \infty$ ; i.e. any small uncertainty in the calibration slope in either channel is dramatically amplified.

Note that, for a realistic range of  $\tau$  (approximately 0.05–0.50), Eqs. (7) can be accurately approximated by the first (linear) term of Taylor's series. In this case the error in  $\alpha$  is represented as an inverse func-

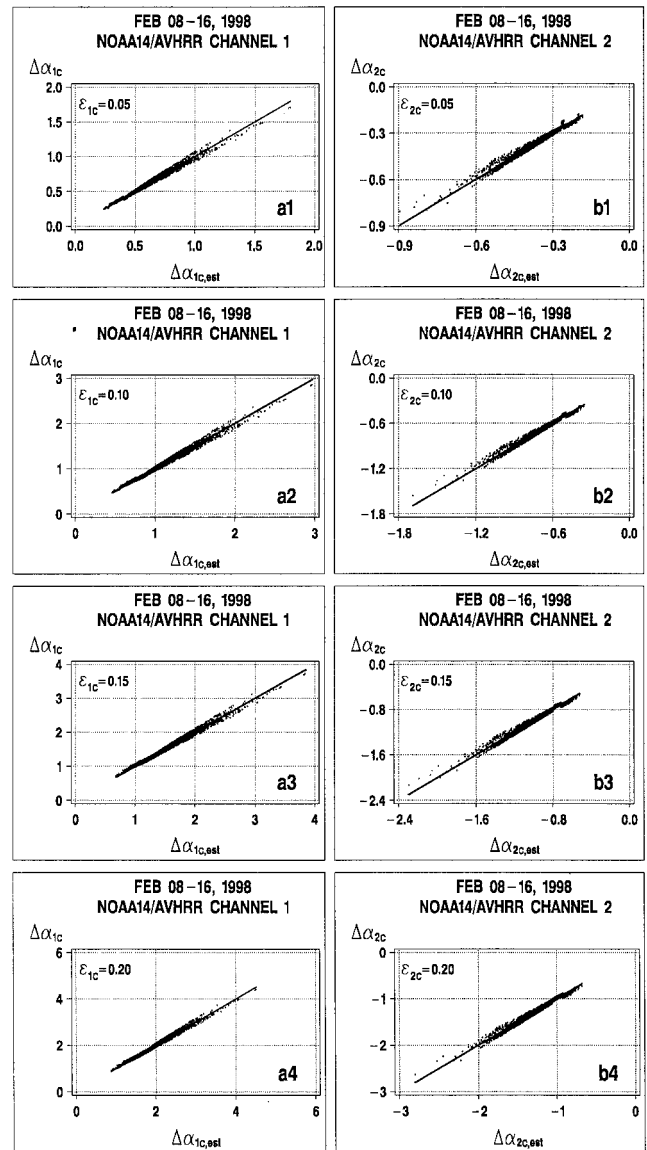


Fig. 7. Ångström exponent perturbations  $\Delta\alpha_i$  resulting from perturbations in the calibration slopes  $\varepsilon_{iC} = \Delta S_i/S_i$  versus those estimated with Eqs. (7),  $\Delta\alpha_{i,est}$ .

tion of  $\tau$ , as was first proposed by Ignatov *et al.*<sup>11</sup> Numerical estimates show that, for  $\tau > 0.1$ , this fit to the logarithmic function in Eqs. (7) is accurate enough to be used for practical quantitative analyses.

### C. Residual Angular Trends in $\Delta\tau_{Ci}$ and $\Delta\alpha_{Ci}$

A high degree of correlation of  $\Delta\tau_{iC}$  and  $\Delta\alpha_{iC}$  with  $\tau_i$  suggests that correlation with any other factors, including Sun-view, scattering, and reflection geometries, is unlikely to be significant. Figure 8 shows  $\Delta\tau_{1C}$  and  $\Delta\tau_{2C}$  relative to various angles for extreme calibration errors,  $\varepsilon_{1C} = \varepsilon_{2C} = +0.20$ . It suggests that the residual angular trends in  $\tau_i$  never exceed  $\sim 0.02$ . The 20% calibration error (chosen here to highlight the amplitudes of the possible angular trends in  $\Delta\tau_{iC}$ , which, if they exist, are proportionate to  $\varepsilon_{iC}$ ), however, appears unrealistic, and the ob-



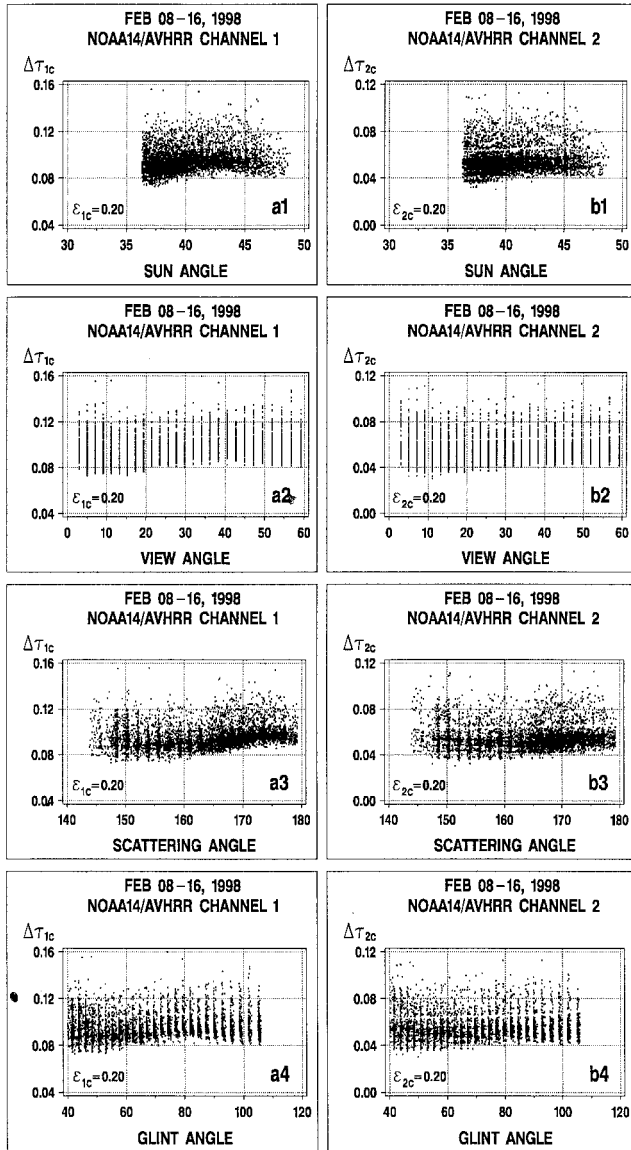


Fig. 8. Perturbations  $\Delta\tau_{iC}$  in aerosol optical depths in AVHRR channels 1 ( $i = 1$ ) and 2 ( $i = 2$ ) versus Sun, view, scattering, and glint angles for a perturbation in the calibration slopes,  $\varepsilon_{iC} = \Delta S_i/S_i = 0.20$ .

served angular amplitude must be scaled in proportion to the real calibration error. For instance, when  $\varepsilon_{iC} \sim 5\text{--}10\%$ , this amplitude is reduced by as many as 4 to as few as 2 times. For many practical applications, this error is beyond the level of detection and may be disregarded.

#### 4. Radiometric Noise and Digitization

##### A. Aerosol Optical Depths

Noise and digitization in albedos were modeled as Gaussian and uniformly distributed signals, as described in Subsection 2.D, and added at the top of the AEROS signal. The two top rows of Fig. 9 show curves of these modeled signals,  $\Delta A_{iX}$  ( $X$  may

be  $N$ ,  $D$ , or  $ND$ ) in AVHRR channels  $i = 1$  (Figs. 9a1 and 9b1) and  $i = 2$  (Figs. 9a2 and 9b2), as they are affected by noise ( $\Delta A_{iN}$ ; Figs. 9a1 and 9a2), digitization ( $\Delta A_{iD}$ ; Figs. 9c1 and 9c2), and their combination ( $\Delta A_{iND}$ ; Figs. 9b1 and 9b2). The two top rows of Table 2 summarize their respective statistics: mean (in all cases,  $|\Delta A_{iX}| < +10^{-4}$ ), standard deviation ( $\sigma_{A_{iX}}$ ), and  $\text{Min}(\Delta A_{iX})/\text{Max}(\Delta A_{iX})$ , where Min and Max are minimum and maximum, respectively. Note that combining a normally distributed  $\Delta A_{iN}$  with a uniformly distributed  $\Delta A_{iD}$  results in an almost perfectly normally shaped  $\Delta A_{iND}$  signal.

The respective two bottom rows of Table 2 and of Fig. 9 show the effect of noise (Figs. 9a3 and 9a4) digitization (Figs. 9b3 and 9b4), and both (Figs. 9c3 and 9c4) on  $\tau_1$  [Eq. (3)] and  $\tau_2$  [Eq. (4)] retrievals. The normal shape of the  $\Delta\tau_{iN}$  curves is expected from the normally distributed  $\Delta A_{iN}$ . Interestingly, the uniformly distributed  $\Delta A_{iD}$  is transformed into a much more Gaussian shaped  $\Delta\tau_{iD}$ . This is so because the retrievals (inversion of  $A_i$  into  $\tau_i$ ) are made under a wide variety of illumination, view, scattering, and reflection geometries, which apparently imparts a normalizing effect to the derived  $\tau$ . The  $\Delta\tau_i$  signal undergoes further evolution toward a Gaussian shape when  $\Delta\tau_{iN}$  and  $\Delta\tau_{iD}$  signals are combined into  $\Delta\tau_{iND}$ , whose curves are already indistinguishable from normal. This fact means that the combined  $ND$  effect on AVHRR aerosol retrievals is equivalent to, and statistically indistinguishable from, the increased Gaussian noise.

Two observations can be made from Table 2. First, in both AVHRR channels ( $i = 1, 2$ ) the respective perturbations are summed up in a rms sense as  $\sigma_{A_{iND}}^2 \approx \sigma_{A_{iN}}^2 + \sigma_{A_{iD}}^2$  and  $\sigma_{\tau_{iND}}^2 \approx \sigma_{\tau_{iN}}^2 + \sigma_{\tau_{iD}}^2$ . Second, in the two AVHRR channels the  $N$  and  $D$  contributions are comparable:  $\sigma_{A_{iN}} \sim \sigma_{A_{iD}}$  and  $\sigma_{\tau_{iN}} \sim \sigma_{\tau_{iD}}$ . This result is an indication of the high quality of the AVHRR radiometric design, in which the two sources of radiometric random errors contribute comparably to the summary error balance. The summary standard deviations of the  $ND$  effect in AVHRR  $\tau$  are  $\sigma_{\tau_{1ND}} \sim 0.8 \times 10^{-2}$  and  $\sigma_{\tau_{2ND}} \sim 1.0 \times 10^{-2}$ . Analyses show no statistically significant trends of  $\Delta\tau_{iN}$ ,  $\Delta\tau_{iD}$ , and  $\Delta\tau_{iND}$  with  $\tau_i$ .

##### B. Ångström Exponent

Figure 10 shows errors in the Ångström exponent that are the result of noise,  $\Delta\alpha_{iN}$  (left); digitization,  $\Delta\alpha_{iD}$  (middle); and their combination,  $\Delta\alpha_{iND}$  (right), which result from the respective effects in separate channels 1 (top) and 2 (middle) and from both effects (bottom). All  $\Delta\alpha_{iX}$  parameters are plotted versus  $\tau_1$ , with the dashed curves marking the boundaries of the  $\pm 3\sigma_{\alpha_{iX}}$  intervals (calculated as explained below).

To better understand Fig. 10, consider  $\tau$  in the two channels as  $\tau_1 + \Delta\tau_{1X}$  and  $\tau_2 + \Delta\tau_{2X}$  (here again,

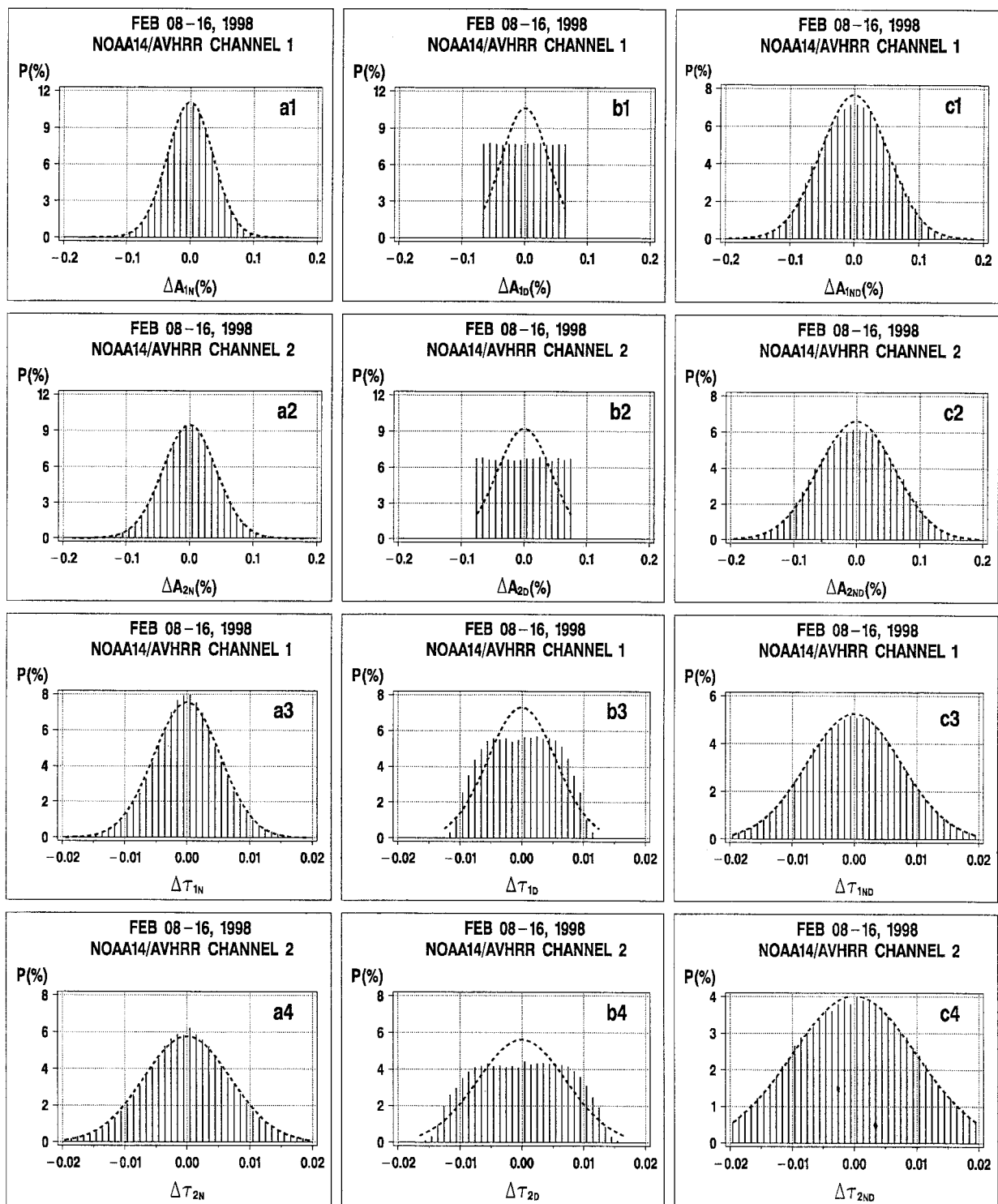


Fig. 9. Top two rows, histograms of perturbation signals superimposed upon the AEROS albedo in AVHRR channels 1 and 2 to imitate noise (a1–a2), digitization (b1–b2), and noise and digitization (c1–c2). Bottom two rows, histograms of the respective aerosol optical depth perturbations.

**Table 2. Statistics of the Noise and Digitization Signals Superimposed upon the Measured Albedo and the Signal's Effect on Aerosol Optical Depth Retrievals**

Title	Channel	Noise	Digitization	Noise + Digitization
Albedo (Min/Max; mean/ standard deviation)	1	-0.159/+0.156; $-7.4 \times 10^{-5}/3.61 \times 10^{-2}$	-0.065/+0.065; $-3.3 \times 10^{-5}/3.75 \times 10^{-2}$	-0.221/+0.201; $-6.0 \times 10^{-5}/5.21 \times 10^{-2}$
	2	-0.185/+0.182; $-8.6 \times 10^{-5}/4.21 \times 10^{-2}$	-0.075/+0.075; $-3.8 \times 10^{-5}/4.33 \times 10^{-2}$	-0.257/+0.234; $-6.9 \times 10^{-5}/6.04 \times 10^{-2}$
AOD (Min/Max; mean/ standard deviation)	1	-0.026/+0.023; $-1.6 \times 10^{-5}/5.25 \times 10^{-3}$	-0.013/+0.013; $-0.8 \times 10^{-5}/5.46 \times 10^{-3}$	-0.032/+0.031; $-0.8 \times 10^{-5}/7.58 \times 10^{-3}$
	2	-0.034/+0.031; $-2.8 \times 10^{-5}/6.90 \times 10^{-3}$	-0.017/+0.017; $-0.8 \times 10^{-5}/5.46 \times 10^{-3}$	-0.041/+0.040; $-2.9 \times 10^{-5}/9.91 \times 10^{-3}$

$X = N, D$ , or  $ND$ ). Perturbation in the Ångström exponent,  $\Delta\alpha_X$ , is then expressed as

$$\begin{aligned}\Delta\alpha_X &= \Lambda \left[ \ln \left( \frac{\tau_1 + \Delta\tau_{1X}}{\tau_2 + \Delta\tau_{2X}} \right) - \ln \left( \frac{\tau_1}{\tau_2} \right) \right] \\ &\equiv \Lambda \left[ \ln \left( 1 + \frac{\Delta\tau_{1X}}{\tau_1} \right) - \ln \left( 1 + \frac{\Delta\tau_{2X}}{\tau_2} \right) \right] \\ &\approx \Lambda \left( \frac{\Delta\tau_{1X}}{\tau_1} - \frac{\Delta\tau_{2X}}{\tau_2} \right); \quad (8)\end{aligned}$$

and its rms deviation,  $\sigma_{\alpha X}$ , as

$$\begin{aligned}\sigma_{\alpha X}^2 &= \Lambda^2 \left( \frac{\sigma_{\tau_{1X}}^2}{\tau_1^2} + \frac{\sigma_{\tau_{2X}}^2}{\tau_2^2} \right) \\ &\equiv \Lambda^2 \left( \frac{\sigma_{\tau_{1X}}^2}{\tau_1^2} + \beta^2 \frac{\sigma_{\tau_{2X}}^2}{\tau_1^2} \right) \\ &\equiv \frac{\Lambda^2}{\tau_1^2} [\sigma_{\tau_{1X}}^2 + \beta^2 \sigma_{\tau_{2X}}^2] \equiv \frac{\sigma_{\alpha X}^{(0)2}}{\tau_1^2}. \quad (9)\end{aligned}$$

Note that only  $\tau_1$  is kept in relation (9), for convenience and compactness of further analysis, whereas  $\tau_2$  was excluded by introduction of a  $\beta$  parameter, defined as  $\beta = \tau_1/\tau_2$  [related to the Ångström exponent as  $\alpha = \Lambda \ln \beta$ , according to Eq. (1)].

Relation (9) explains, in particular, the increased scatter in the Ångström exponent perturbation,  $\Delta\alpha_X$  when  $\tau \rightarrow 0$ , as observed in Fig. 10. Relation (9) further suggests that the scatter increases in inverse proportion to  $\tau$ . The inverse value of  $\tau_1$ ,  $1/\tau_1$ , was therefore binned;  $\sigma_{\alpha X}$  was calculated for each bin separately and plotted in Fig. 11 as a function of  $1/\tau_1$ . The empirical points fall well along the straight lines, as predicted by relation (9), whose slopes,  $\sigma_{\alpha X}^{(0)}$  are shown in the respective parts of Fig. 11. Note that these slopes were substituted into relation (9) to calculate the  $\pm 3\sigma_\alpha$  lines in Fig. 10.

Figure 11 estimates and compares individual contributions from the three effects ( $N$ ,  $D$ , and  $ND$ ) and from different channels ( $i = 1, 2$ ) to the uncertainty of the Ångström exponent. The combined effect is determined by summing of the respective individual terms in a rms sense, similarly to treatment of the albedo and AOD perturbations. In particular, values of  $\sigma_{\alpha X}^{(0)}$  in the top and middle rows of the figure (or in Figs. 11a1 and 11b1 and Figs. 11b1 and 11b2)

sum in a rms sense, to produce  $\sigma_{\alpha X}^{(0)}$  found in the bottom row (or in Figs. 11c1–11c3). For example, a combined rms  $\alpha$  perturbation that results from noise [ $\sigma_{\alpha 1N}^{(0)} = 0.021$ ; Fig. 11a1] and from digitization [ $\sigma_{\alpha 1D}^{(0)} = 0.021$ ; Fig. 11b1] in channel 1 is found as  $\sigma_{\alpha 1ND}^{(0)} = (0.021^2 + 0.021^2)^{1/2} \approx 0.029$  (Fig. 11c1). Similarly, a combined rms perturbation in the Ångström exponent that results from noise in channel 1 [ $\sigma_{\alpha 1N}^{(0)} = 0.021$ ; Fig. 11a1] and in channel 2 [ $\sigma_{\alpha 2N}^{(0)} = 0.030$ ; Fig. 11a2] is found as  $\sigma_{\alpha N}^{(0)} = (0.021^2 + 0.030^2)^{1/2} \approx 0.037$ .

The contributions to  $\sigma_{\alpha ND}^{(0)}$  from noise and digitization are nearly similar, as was the case with  $\sigma_{\tau ND}$ , additionally confirming the balanced radiometric design of the AVHRR. Channel 2 contributes  $\sim 1.5$  times more than channel 1 in all cases. This is because of the combined effect of two different mechanisms. First, the calibration slope is generally higher in channel 2 than in channel 1 (to which both the  $N$  and the  $D$  signals are proportional). Second, the value of  $\tau_2$  is generally lower than that of  $\tau_1$ . Both lead to a higher noise-to-signal ratio in this channel,  $\sigma_{\tau 2ND}/\tau_2 > \sigma_{\tau 1ND}/\tau_1$ .

### C. Angular Trends in $\Delta\tau$ and $\Delta\alpha$

Figure 12 shows statistics (mean, standard deviation, min, and max) of  $\tau$  perturbations in channels 1 (Figs. 12a1–12a4) and 2 (Figs. 12b1–12b4) and the Ångström exponent derived therefrom (Figs. 12c1–12c4) for four different angles. The mean is always close to zero, as expected. The most notable trends are observed in the view angle. Somewhat smaller trends are observed for glint and scattering angles, and no trend is seen for Sun angle. Trends in  $\Delta\alpha$  are an exaggerated mirror image of those in  $\Delta\tau$ , as relation (8) shows. The two images are correlated; the Ångström exponent is more sensitive to uncertainties than is  $\tau$ . The observed angular features are theoretically analyzed and discussed in more detail in Section 5.

## 5. Theoretical Analysis with a Simplified Radiative Transfer Equation

In this section we employ a theoretical analysis based on a linearized single-scattering radiative transfer equation to better understand the empirical results obtained in Sections 3 and 4 and to permit their

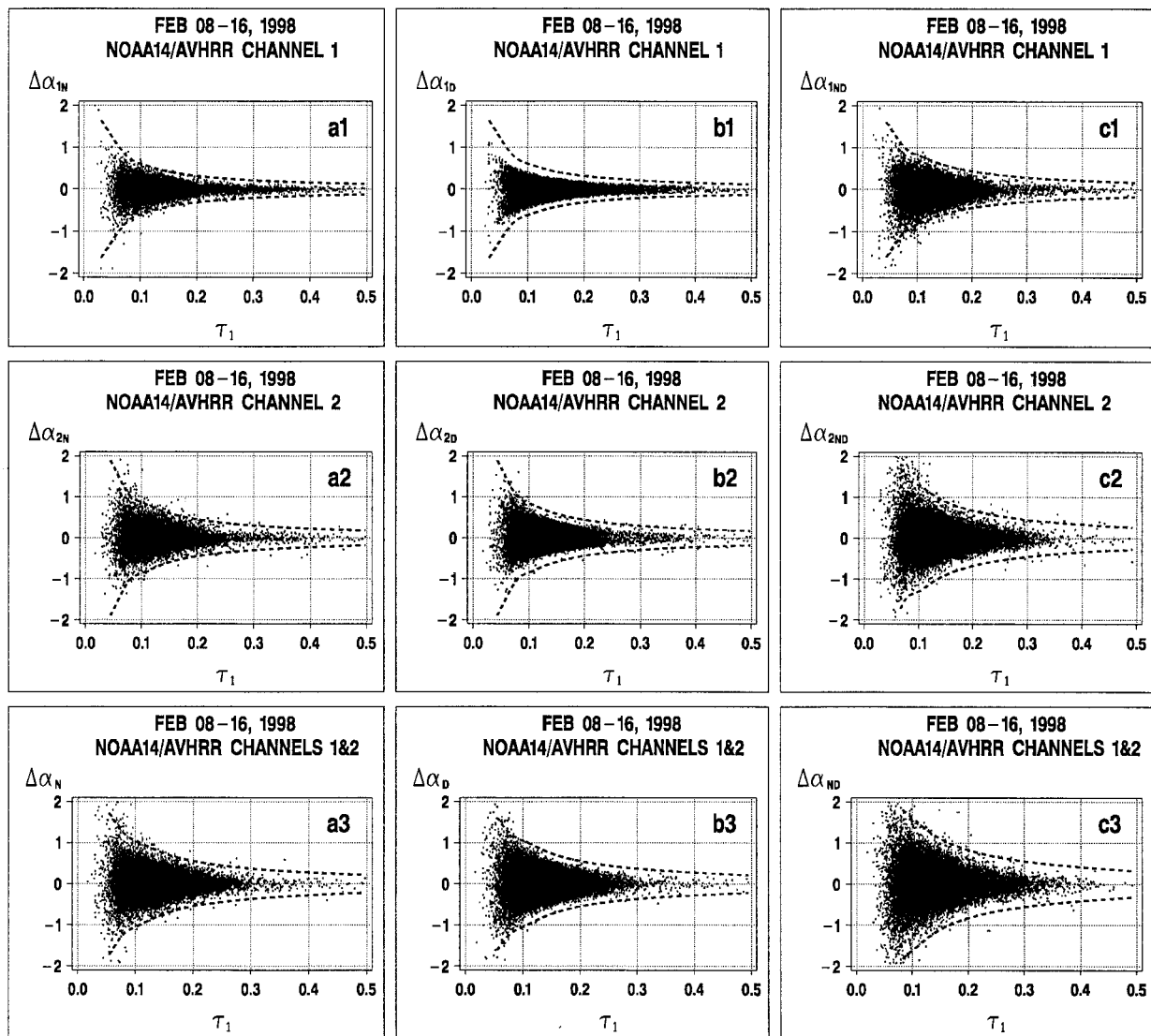


Fig. 10. Ångstrom exponent perturbations  $\Delta\alpha_{IX}$  caused by a, noise, b, digitization, and c, noise and digitization in AVHRR channel (1), channel 2 (2), and both (3) versus  $\tau_1$ . The  $\pm 3\sigma_\alpha$  (dashed) lines are drawn from the data in respective panels of Fig. 11.

generalization for use with other sensors and channels.

#### A. Single-Scattering Approximation of the Radiative Transfer Equation

Reflectance factor  $\rho$  (customarily used in the literature that treats ocean color and atmospheric optics and related to the albedo introduced above as  $\rho_i = A_i/\mu_S$ , where  $\mu_S = \cos \theta_S$  and  $\theta_S$  is the Sun's zenith angle), at the top of the ocean atmosphere system is represented as<sup>33,34</sup>

$$\rho_i = (\rho_i^R + \rho_i^A + \rho_i^S \times T_i) t_i^g, \quad \rho_i^R = \frac{p^R(\chi) \tau_i^R}{4\mu_S \mu_V},$$

$$\rho_i^A = \frac{\omega_i^{At} p_i^{At}(\chi) \tau_i^t}{4\mu_S \mu_V}, \quad (10)$$

where  $i$  is the channel;  $\rho_i^R$  and  $\rho_i^A$  are Rayleigh and the aerosol contributions, respectively, to the mea-

sured reflectance factor,  $\mu_V = \cos \theta_V$ ,  $\theta_V$  is the view zenith angle,  $\chi$  is the scattering angle;  $p^R(\chi) = 0.75(1 + \cos^2 \chi)$  is the Rayleigh phase function (the same in the two channels);  $\tau_i^R$  are Rayleigh optical depths in the channels [ $\tau_1^R \approx 0.0555$ ,  $\tau_2^R \approx 0.0180$  for the NOAA-14 AVHRR (Ref. 2)]; and  $p_i^{At}(\chi)$ ,  $\omega_i^{At}$ , and  $\tau_i^t$  are the aerosol phase function, the albedo of single scattering, and the optical depth in channel  $i$ , respectively. All aerosol parameters may vary from one retrieval point to another, as is manifested in Eqs. (10) by introduction of the superscript  $t$  (true) to differentiate these parameters from those prescribed in the retrieval model [ $p_i^A(\chi)$ ,  $\omega_i^A$ ] and from the AOD estimated with their use,  $\tau_i$ .

The  $(\rho^S T)_i$  term is due to the ocean's diffuse (Lambertian) reflectance,  $\rho_i^S$  [ $\rho_1^S = 2.0 \times 10^{-3}$ ;  $\rho_2^S = 0.5 \times 10^{-3}$  (Ref. 2)] attenuated by scattering in the atmosphere on both molecules and particles. According to, e.g., Viollier *et al.*,<sup>33</sup> the atmospheric dif-



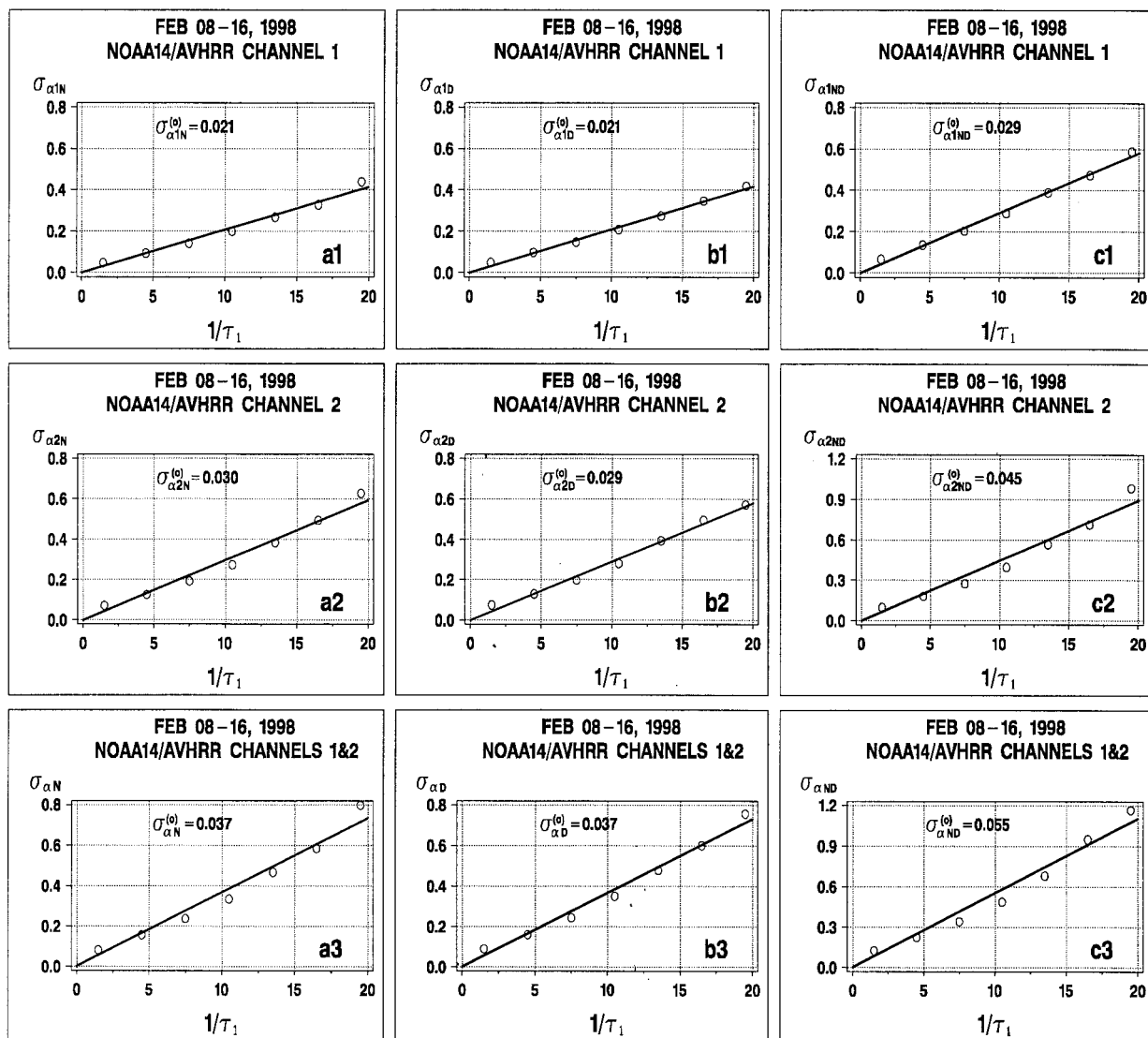


Fig. 11. Root mean square deviation of the Ångström exponent perturbations from the data in the respective panels of Fig. 10.

fuse transmittance can be estimated as  $T_i \approx \exp[-(1/\mu_S + 1/\mu_V)(0.5\tau_i^R + 0.13\tau_i)]$ . Numerical estimates for  $\mu_S = 0.5 \dots 1.0$  and  $\mu_V = 0.5 \dots 1.0$  give  $T_1 \sim 0.75 \pm 0.20$  in channel 1 ( $\tau_1^R = 0.0555$ ,  $\tau_1^A \sim 0 \dots 1.0$ ) and  $T_2 \sim 0.78 \pm 0.20$  in channel 2 ( $\tau_2^R = 0.0180$ ,  $\tau_2 \sim 0 \dots 1.0$ ). For typical retrieval Sun-view geometries, this inequality holds:  $(\rho^S T)_i \ll \rho_i^R$ . Its individual terms are estimated as  $(\rho^S T)_1 \sim 2.0 \times 10^{-3} \times (0.75 \pm 0.20) \sim (1.5 \pm 0.4) \times 10^{-3}$ ,  $(\rho^S T)_2 \sim 0.5 \times 10^{-3} \times (0.78 \pm 0.20) \sim (0.4 \pm 0.1) \times 10^{-3}$ , and  $\rho_1^R \sim (1.3 \pm 0.2) \times 6 \times 10^{-2} \sim (7.8 \pm 1.2) \times 10^{-2}$ ,  $\rho_2^R \sim (1.3 \pm 0.2) \times 2 \times 10^{-2} \sim (2.6 \pm 0.4) \times 10^{-2}$ . [Here, to facilitate making an estimate, we set  $P^R(\chi)$  to  $1.3 \pm 0.2$  in backscatter, which is typical of AVHRR scattering geometry for the four data sets used in this study.] The surface-to-Rayleigh ratio is  $(\rho^S T)_1/\rho_1^R \sim (1.9 \pm 0.8) \times 10^{-2}$  in the first channel and  $(\rho^S T)_2/\rho_2^R \sim (1.5 \pm 0.6) \times 10^{-2}$  in the second. The diffuse reflectance term thus contributes a few of a percent to the measured signal when no aerosol is

present in the retrieval scene, and this contribution decreases as the aerosol is introduced and its concentration increases. In the analyses below, the ocean diffuse reflectance term was neglected to simplify the theoretical formulas, with little loss of accuracy.

The term  $t_g$  is due to gaseous absorption in the atmosphere. It is approximated as  $t_g \sim \exp[-(1/\mu_S + 1/\mu_V)\tau_i^g]$ , where  $\tau_i^g$  is gaseous optical depth.<sup>33</sup> Note that formulation of Eqs. (10) assumes that all absorbers are fully placed above the scattering layer. This approximation largely holds in channel 1, in which the major absorber is ozone, which is located at an approximate altitude of 18–20 km. Together with two other (minor) absorbers, water vapor and oxygen,  $\tau_1^g$  is  $\sim 0.04$  for NOAA-14, for tropical-midlatitude concentrations of the respective gases.<sup>2</sup> For the same ranges of geometry as considered above ( $\mu_S = 0.5 \dots 1.0$  and  $\mu_V = 0.5 \dots 1.0$ ), one obtains that, in channel 1,  $\tau_1^g \sim 0.88 \pm 0.04$ . In channel 2 the main absorber is water vapor, and the minor

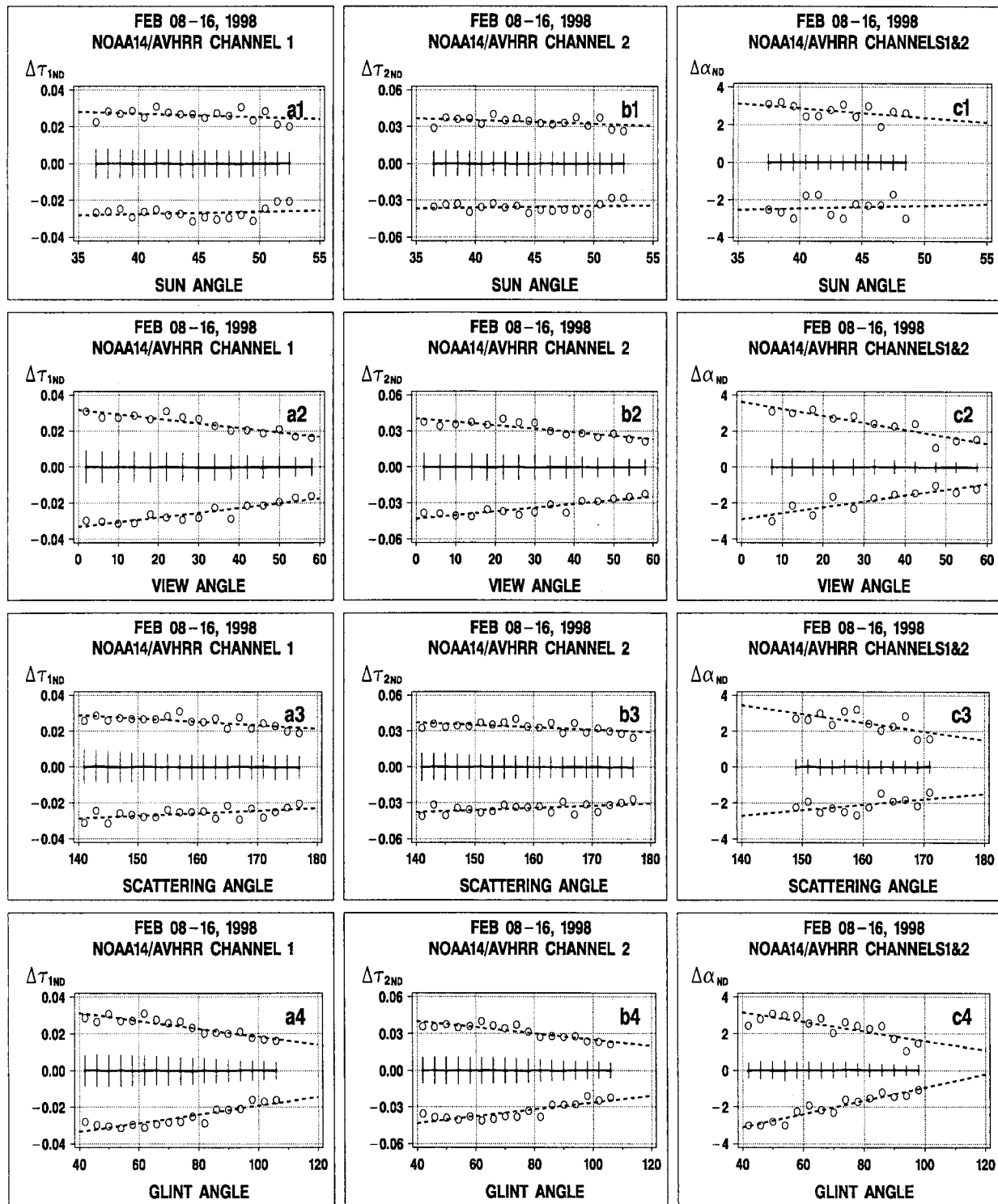


Fig. 12. Statistics (mean, standard deviation, and min/max) of perturbations  $\Delta\tau_{1ND}$  in aerosol optical depths owing to noise and digitization in AVHRR channels 1 (a1–a4) and 2 (b1–b4) and Angstrom exponent  $\Delta\alpha_{ND}$  versus Sun view, and scattering, and glint angles (c1–c4).

absorber is oxygen. Together, they amount to  $\tau_2^g \sim 0.17$  for NOAA-14 and tropical atmosphere. Both absorbers are, as a rule, well mixed with aerosols in the lower troposphere. Therefore their concentrations need to be adjusted accordingly, before the formulation of Eqs. (10) can be used in quantitative

estimates. A value of  $\tau_2^g \sim 0.08$  was adopted in the numerical estimates below; a uniform mixture was assumed. For the same ranges of geometry as above,  $t_2^g \sim 0.79 \pm 0.06$ .

Rewriting Eqs. (10) in albedo units for consistency with Sections 3 and 4 and omitting channel index  $i$  for

brevity yield

$$A = (A^R + A^A)t^g, \quad A^R = \frac{p^R(\chi)\tau^R}{4\mu_V},$$

$$A^A = \frac{\omega^{At}p^{At}(\chi)\tau^t}{4\mu_V} \equiv \frac{p^A(\chi)\tau}{4\mu_V}. \quad (10a)$$

From Eqs. (10a) the following formulas for  $\tau^t$  and its retrieval  $\tau$  are obtained:

$$\tau^t = \frac{1}{[\omega p(\chi)]^{At}} \left[ 4\mu_V \times \frac{A}{t^g} - p^R(\chi)\tau^R \right],$$

$$\tau = \frac{1}{p^A(\chi)} \left[ 4\mu_V \times \frac{A}{t^g} - p^R(\chi)\tau^R \right]. \quad (11)$$

In Eqs. (10a) and (11), the conservative ( $\omega = 1$ ) model aerosol phase function  $p^A(\chi)$ , that was used in the retrievals was introduced to differentiate this phase function from the true one,  $[\omega p(\chi)]^{At}$ , which may vary from one retrieval point to another. As a result, estimated aerosol optical depth  $\tau$  and its increment  $\Delta\tau$  may differ from the true ones,  $\tau^t$  and  $\Delta\tau^t$ , by a factor equal to the ratio of the respective phase functions.

From Eqs. (11), a perturbation in aerosol optical depth  $\Delta\tau$  that resulted from a perturbation in albedo  $\Delta A$  is calculated as

$$\Delta\tau^t = \frac{4\mu_V}{\omega^{At}p^{At}(\chi)} \frac{\Delta A}{t^g}, \quad \Delta\tau = \frac{4\mu_V}{p^A(\chi)} \frac{\Delta A}{t^g}. \quad (12)$$

Below, two types of perturbation  $\Delta A$  in albedo, multiplicative (calibration slope error) and additive (noise and digitization), are considered separately.

#### B. Effect of Calibration Slope Uncertainty on $\tau_i$ and $\alpha$

Calibration slope error  $\varepsilon_C$  results in an albedo error that is proportional to the albedo itself:  $\Delta A = \varepsilon_C A$ . Substituting this equation into the right-hand sides of Eqs. (12), along with the formula for albedo from Eqs. (10a), one obtains

$$\Delta\tau = \left[ \tau + \tau^R \frac{p^R(\chi)}{p^A(\chi)} \right] \varepsilon_C. \quad (13)$$

The structure of Eq. (13) is identical to that of Eqs. (5). Both equations suggest that the perturbation in  $\tau$  is proportional to the percent perturbation in albedo and that the proportionality coefficient [the aggregate in brackets in Eq. (13)] has two terms, one of which is proportional to  $\tau$  and one that does not depend on  $\tau$ . Comparing Eqs. (4) and (5) with Eq. (13) suggests that

$$b_0 = 1, \quad a_0 = \frac{p^R(\chi)}{p^A(\chi)} \tau^R. \quad (14)$$

Equations (13) and (14) thus predict that  $b_0 = 1$  (and does not depend on the aerosol retrieval model) and that theoretical factor  $a_0$  will be proportional to the Rayleigh optical depth. Table 1 shows, however,

that the empirically estimated  $b_0$  is  $\sim 0.71 \pm 0.02$  in channel 1 and  $\sim 0.74 \pm 0.03$  in channel 2, whereas  $a_0$  in channels 1 ( $0.370 \pm 0.011$ ) and 2 ( $0.158 \pm 0.004$ ) differ by a factor of ( $2.35 \pm 0.13$ ). That value is somewhat lower than the theoretically expected one,  $\sim 3.1$ , based on the ratio of respective Rayleigh optical depths in the channels. Besides Rayleigh optical depths, parameter  $a_0$  is also expected to depend on values of  $p^A(\chi)$ , which differ only slightly in the channels. In channel 1 the empirical  $a_0 \sim 0.37 \pm 0.01$  is less than the theoretical estimate from Eqs. (14),  $a_0 \sim 0.52 \pm 0.08$ , by  $\sim (30 \pm 20)\%$ . In channel 2 the empirical  $a_0 \sim (0.158 \pm 0.004)$  is less than the theoretical estimate,  $\sim (0.18 \pm 0.02)$ , by  $\sim (13 \pm 14)\%$ .

Theoretical Eqs. (13) and (14) overestimate both  $a_0$  and  $b_0$  consistently by tens of percent. Part of this disagreement may be due to multiple scattering effects that are not considered in the present single-scattering formulation. Another part may be due to calibration errors that may be already be present in the original AEROS data. The theoretical relationships thus closely reproduce the empirical results qualitatively, but their parameters require fine tuning (up to a few tenths of a percent) if the theoretical estimates are to be used for quantitative analyses.

The theoretical Ångström exponent (and its perturbation) is derived from the respective  $\tau$  (and their perturbations) from Eqs. (1), (6), and (7). This derivation is trivial and is therefore omitted here.

#### C. Effect of Noise and Digitization on $\tau_i$ and $\alpha$

We estimate the perturbations in  $\tau$ ,  $\Delta\tau_X$ , that are due to noise, digitization, or their combination ( $X = N, D, ND$ , respectively) by substituting  $\Delta A_X$  into Eqs. (12):

$$\Delta\tau_X = \frac{4\mu_V}{p^A(\chi)} \frac{\Delta A_X}{t^g}. \quad (15)$$

Figure 13 compares  $\Delta\tau_X$ , estimated with the simple analytical equation (15), with the accurate lookup-table inversions. The agreement between theoretical and empirical results is quite good and suggests that Eq. (15) can be used not only for qualitative analyses of the  $N$  and  $D$  effects on the retrievals but even for the quantitative prediction of the effects. The mean error,  $\langle \Delta\tau_X \rangle$ , and its rms deviation,  $\sigma_{\tau_X}$ , are calculated as

$$\langle \Delta\tau_X \rangle = 0, \quad \sigma_{\tau_X} = \frac{4\mu_V}{p^A(\chi)} \frac{\sigma_{AX}}{t^g}. \quad (16)$$

Equations (15) and (16) relate perturbations in  $\tau$ ,  $\Delta\tau_X(\sigma_{\tau_X})$ , to perturbations in albedo,  $\Delta A_X(\sigma_{AX})$ . (Recall that the frequency distributions of  $\Delta A_{iX}$  are shown in the two top parts of Fig. 9.) According to Eqs. (15) and (16),  $\Delta A_{iX}$  are additionally modulated by the variable Sun, view, and scattering geometries, aerosol type, and gaseous absorption [ $\mu_V$ ,  $p^A(\chi)$ , and  $t_g$  in Eqs. (15) and (16)]. Numerical estimates show that  $p^A(\chi)$  and  $t_g$  contribute relatively little to the angular trend in  $\Delta\tau_X$ , so the approximate proportionality takes place between  $\Delta\tau_X(\sigma_{\tau_X})$  and  $\mu_V$ . This the-

oretical fact is consistent with the viewing angle trend illustrated in Figs. 12a2–12c2. [Note that the glint angle trends in  $\Delta\tau_X(\sigma_{\tau_X})$  shown in Figs. 12a4–12c4 stem from high correlation observed between the view and glint angles in the data.]

An interesting feature of Eqs. (15) and (16) and the empirical results of Section 3 is a seeming violation of the reciprocity principle, as  $\Delta\tau_X(\sigma_{\tau_X})$  depend differently on the viewing angle and the Sun angle. This is so because it is the radiance (or albedo) that is subject to an additive error caused by noise and digitization. These sources of error need to be further normalized to the Sun angle to become reflectances, which, according to radiative transfer equations (10), reveal actual reciprocity. Therefore the different sensitivities of  $\Delta\tau_X(\sigma_{\tau_X})$  to Sun and view angles are expected.

We can obtain a theoretical estimate of the Ångström exponent error that results from AOD errors by substituting the theoretical  $\Delta\tau_X(\sigma_{\tau_X})$  from Eqs. (15) and (16) into Eqs. (8) and (9). Inasmuch as Fig. 13 suggests that the empirical  $\Delta\tau_X$  are closely reproduced theoretically, the theoretical  $\Delta\alpha_X$  are also close to the empirical  $\Delta\alpha_X$  analyzed in Section 4.

## 6. Implications of Errors for the AVHRR Aerosol Information Content

Radiometric errors depreciate the information content of aerosol retrievals from the AVHRR. The degree of this depreciation is estimated below through the “relative uncertainty” of a measurement (this term was proposed by one of the anonymous reviewers of this paper). This concept was introduced for the vertical soundings of atmospheric temperature and humidity profiles<sup>35,36</sup> and later applied to sea-surface temperatures.<sup>37</sup> Here we use it further to assess quantitatively the AVHRR aerosol information content.

### A. Relative Uncertainty and Information Content

The information content of a measurement  $\mathcal{P}_M$ , with its measurement uncertainty  $\varepsilon_{\mathcal{P}_M}$  (customarily characterized by its standard deviation  $\sigma_{\mathcal{P}_M}$ ), should be judged by the new information that it adds to the *a priori* information already known about parameter  $\mathcal{P}$  from past measurements (for instance, climatological mean  $\langle\mathcal{P}_C\rangle$  and standard deviation  $\sigma_{\mathcal{P}_C}$ ).<sup>35,36</sup> Rodgers<sup>36</sup> suggests that  $\mathcal{P}_C$  be regarded as a “virtual measurement” and treated in exactly the same way as the actual measurement  $\mathcal{P}_M$ . In particular, the two could be further combined if one used  $(1/\sigma_{\mathcal{P}_M})^2$  and  $(1/\sigma_{\mathcal{P}_C})^2$  as their respective weights. The relative uncertainty of a measurement,  $\eta = \varepsilon_{\mathcal{P}_C}/\varepsilon_{\mathcal{P}_M}$ , is thus an indicator of the measurement’s information content. In particular,  $\eta = 1$  means that the error in the parameter being retrieved is comparable with the *a priori* uncertainty. For an arbitrary  $k > 1$ ,  $\eta = k$  means that no more than  $k$  classes (gradations) can be reliably distinguished in the data.

Note that  $\eta$  is not only a measure of the current measurement error. Neither is it only a measure of the current *a priori* uncertainty. Rather, it repre-

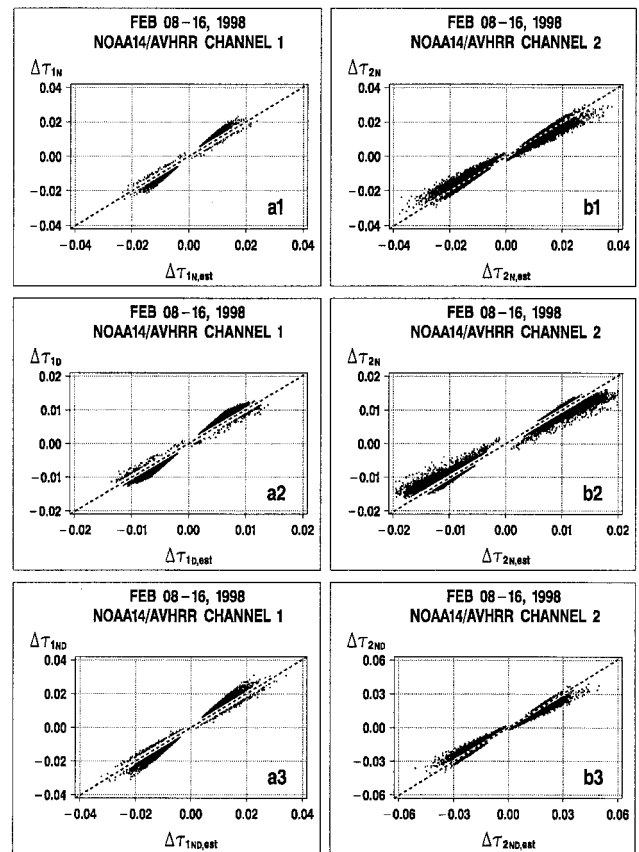


Fig. 13. Perturbations  $\Delta\tau_{iX}$  in aerosol optical depths owing to noise ( $X = N$ ; a1–b1), digitization ( $X = D$ ; a2–b2), and noise and digitization ( $X = ND$ ; a3–b3) in AVHRR channels 1 and 2, estimated with exact lookup-table inversions, versus those estimated with Eq. (15).

sents their relative proportion, which may change as the *a priori* uncertainty ( $\sigma_{\mathcal{P}_C}$ ) is reduced while new data become available, measurement accuracy ( $\sigma_{\mathcal{P}_M}$ ) improves, or both. For instance, Aoki<sup>37</sup> pointed out that a measurement would be more informative when only annual climatology data were available rather than when a more detailed monthly climatology were available.

Interpretation of parameter  $\eta$  may be different for different types of measurement error. In the case of radiometric noise and digitization, parameter  $\eta$  characterizes the (relative) degree of blurriness in the instantaneous field of a parameter, in its short-term time series, or both, suggesting how many shades can be reliably separated in the data. For calibration errors, parameter  $\eta$  characterizes the (relative) strength of systematic error in the data. For stability error, parameter may serve as a measure of our ability to detect long-term trends in the data, e.g., for climate-related applications.

### 1. Definitions of Aerosol Uncertainties

In this study the uncertainty is measured in a rms sense,  $\sigma_{\mathcal{P}}$ , for normally distributed values and through the range  $\delta\mathcal{P}$  for any other type of frequency



distribution. (For normally distributed values, note a useful relationship  $\delta\mathcal{P} \sim 6\sigma_{\mathcal{P}}$ , which results from variability of  $\pm 3\sigma_{\mathcal{P}}$  about the mean  $\langle\mathcal{P}\rangle$ ). According to analyses of O'Neill *et al.*<sup>38</sup> and Ignatov and Stowe,<sup>32</sup>  $\log \tau$  is distributed normally, and therefore parameter  $\mathcal{P}$  is better defined as  $\mathcal{P} = \log \tau$ . The Ångström exponent,  $\alpha$ , is distributed normally,<sup>32</sup> and therefore  $\mathcal{P} = \alpha$ .

## 2. Aerosol A Priori Uncertainty

The climatology of a parameter  $\mathcal{P}$  is customarily represented by its mean,  $\langle\mathcal{P}_C\rangle$ , and its standard deviation,  $\sigma_{\mathcal{P}_C}$ , on a space–time grid (e.g., 1° monthly sea surface temperatures).<sup>39</sup> Space–time stratified aerosol climatology is not yet available. It is being developed in the framework of the GACP.<sup>4</sup> In this study the *a priori* aerosol uncertainty is thus defined through the variability of the respective aerosol parameters within the four data sets, each covering the global belt of 5–25 °S within 9-day periods.<sup>32</sup>

According to Ignatov and Stowe,<sup>32</sup>  $\tau$  is distributed log-normally, with a typical geometric mean and a standard deviation of  $\tau_g \sim 0.15$  and  $\mu \sim 1.5$ , respectively (see Ref. 38 for the definitions). The  $\pm 3\sigma$  interval in a  $\log \tau$  space is thus defined as  $(\tau_g/\mu^3; \tau_g\mu^3) \sim (0.04; 0.50)$ . For the numerical estimates below, the value of range,  $\delta\tau = 0.46$ , was thus used. Ångström exponent  $\alpha$  is distributed normally, with a rms deviation  $\sigma_{\alpha 0} = 0.22 \pm 0.02$  that is equivalent to a range of variability of  $\delta\alpha \sim 6\sigma_{\alpha 0} \sim 1.3 \pm 0.1$ .<sup>32</sup>

For the analysis of climate change in  $\tau$  or  $\alpha$ , aerosol *a priori* uncertainty should be defined through the long-term trends in the parameter to be detected. In what follows, trends in  $\delta\tau_S$  and  $\delta\alpha_S$  are estimated that correspond to an  $S$  error of  $\varepsilon_S = 1\%$ .

## 3. Aerosol Measurement Uncertainty

The *ND* radiometric errors depend on the sensor's performance, vary from one point to another, and depend on Sun and view geometries. In addition to these factors, the  $C$  and  $S$  errors depend also on  $\tau$ . In the numerical estimates below, typical AVHRR radiometric errors, for typical AVHRR Sun and view geometries, are used.

The two types of error—systematic (the  $C$  and  $S$  errors) and random (the *ND* errors)—may require different mathematical treatment and interpretation. The systematic  $C$  and  $S$  errors are measured by their magnitude, whereas the normally distributed random *ND* errors are defined through either their standard deviations ( $\sigma_{\tau_{iND}}$ ,  $\sigma_{\alpha_{iND}}$ ) or ranges ( $\delta\tau_{iND} \sim 6\sigma_{\tau_{iND}}$ ,  $\delta\alpha_{iND} \sim 6\sigma_{\alpha_{iND}}$ ). Note that only a combined *ND* effect in both  $\tau_1$  and  $\tau_2$  is considered, as is a combined effect of both channels 1 and 2 in  $\alpha$ , as they are of most practical interest.

### B. Calibration and Stability Errors

#### 1. $\tau$ -Calibration Error

Equations (5) suggest that  $\Delta\tau_{iC}$  depend on variable  $\tau_i$ . The degree of this dependence is characterized by the factor in brackets in Eqs. (5), which varies by approx-

imately a factor of 2 in channel 1 (from 0.37 to 0.73) and by approximately a factor of 3 in channel 2 (from 0.16 to 0.53) when  $\tau_i$  increases from 0 to 0.5. As a result, the calibration error at the high-end  $\tau_1$  ( $\tau_2$ ) is a factor of  $\sim 2$  ( $\sim 3$ ) greater than that at the low-end  $\tau_1$  ( $\tau_2$ ).

Equations (5) also suggest that  $\Delta\tau_{iC}$  are directly proportional to  $\varepsilon_{iC}$ . The best-case calibration errors (see Section 2 for details) are  $\varepsilon_{1C} = \pm 5\%$  ( $\Delta\tau_{1C} \sim \pm 0.019/0.037$  for the low–high-end  $\tau_1$ ) and  $\varepsilon_{2C} = \pm 7\%$  ( $\Delta\tau_{2C} \sim \pm 0.011/0.037$  for the low–high-end  $\tau_2$ ). From these estimates,  $\eta_{\tau 1C} \equiv \delta\tau/(2\Delta\tau_{1C})$  ranges from  $\sim 13$  (low-end  $\tau_1$ ) to  $\sim 7$  (high-end  $\tau_1$ ), and  $\eta_{\tau 2C} \equiv \delta\tau/(2\Delta\tau_{2C})$  ranges from  $\sim 22$  (low-end  $\tau_2$ ) to  $\sim 7$  (high-end  $\tau_2$ ). (The factor of 2 was introduced to account for the  $\pm$  in the calibration uncertainty.) These results suggest that, on average, reliable separation of approximately 10 to 20 classes in  $\tau$  is possible.

#### 2. $\alpha$ -Calibration Error

Equations (7) suggest that  $\Delta\alpha_{iC}$  increases [whereas  $\eta_{\alpha iC} = \delta\alpha/(2\Delta\alpha_{iC})$  decreases] toward low  $\tau_i$ . For the best-case calibration errors,  $\eta_{\alpha 1C} = 1$  when  $\tau_{1C}^{(0)} \sim 0.11 \pm 0.01$  in channel 1 ( $\varepsilon_{1C} = \pm 5\%$ ,  $\varepsilon_{2C} = 0$ ) and  $\eta_{\alpha 2C} = 1$  when  $\tau_{2C}^{(0)} \sim 0.08 \pm 0.01$  in channel 2 ( $\varepsilon_{1C} = 0$ ,  $\varepsilon_{2C} = \pm 7\%$ ). Calibration uncertainties, however, are present in both AVHRR channels. If they are counterdirected (i.e.,  $\varepsilon_{1C}$  and  $\varepsilon_{2C}$  have opposite signs), the errors add and the actual  $\tau_{iC}^{(0)} \sim 0.2$ ; if they are codirected (i.e.,  $\varepsilon_{1C}$  and  $\varepsilon_{2C}$  have the same sign, which is more likely if the same vicarious calibration technique is applied consistently to calibration of both channels), then errors from different channels may offset each other, so the errors in the Ångström exponent will partially cancel. For instance, Ignatov and Stowe<sup>32</sup> found no notable systematic error in the retrieved Ångström exponent.

#### 3. $\tau/\alpha$ -Stability Errors

When  $\varepsilon_{1S} = \varepsilon_{2S} = +1\%$ ,  $\Delta\tau_{1S}$  is  $\sim 0.004/0.007$  and  $\Delta\tau_{2S}$  is  $\sim 0.002/0.007$  (for  $\tau_i = 0.0/0.5$ ). Over the lifetime of a NOAA satellite, and during switches from one satellite to another, the error may reach a few percent, so artifacts in the  $\tau_i$  time series of a few hundredths are expected. Stowe *et al.*<sup>30</sup> observed trends–discontinuities in the PATMOS data set  $\tau_1$  time series of approximately this magnitude, which they attributed to the residual calibration problems.

The error in the Ångström exponent varies in approximately inverse proportion to  $\tau$ , so it is not defined at  $\tau_i = 0$ . When  $\tau_i = 0.1/0.2$  (typical aerosol loadings for the four data sets used in this study),  $\Delta\alpha_{1S} \sim 0.15/0.10$  and  $\Delta\alpha_{2S} \sim 0.10/0.07$ . A few-percent AVHRR instability would thus lead to artifacts in the  $\alpha$  time series of an order of  $\sim 0.5$ , which is comparable with the range of its natural variability ( $\sim 2$ ).

#### 4. Improving the Relative Uncertainty

Calibration-related error is systematic. Potentially it may be adjusted for empirically, by use of ground measurements in a few anchor points. If ground

measurements are not available, one may adjust the retrievals by setting the empirical frequency distribution to a position expected from the available *a priori* knowledge of aerosols that is specific for the area and season under consideration (e.g., climatology). Note, however, that this approach can be employed if the calibration, however uncertain, is stable over the space–time box covering the measurements.

The numerical estimates here support the conclusion reached at by Brest *et al.*<sup>24</sup> that the “real decadal-scale changes of the earth are much smaller in magnitude than uncertainties in calibration changes and cannot be reliably detected without significant improvements of instrument calibration.” More realistically, it is the high sensitivity of aerosol retrievals (and, in particular, of the Ångström exponent) to the calibration uncertainties that can be used to ensure the stability of the AVHRR calibration with a better accuracy than is now achievable with the calibration techniques based on radiances (cf. Evans and Gordon,<sup>40</sup> who used the time series of water-leaving radiances from the Coastal Zone Color Scanner to examine the stability of its calibration retrospectively). The accuracy of such a vicarious calibration is expected to be progressively greater in proportion to the size of the data sets to which it is applied (a global aggregate is preferable). After being calibrated in a global sense, the data can be used for exploring seasonal and regional redistribution of aerosol characteristics, assuming that their global conglomerate is nonvariable. For monitoring relatively large regional and seasonal signals in  $\tau$ , the low-end  $\tau$  may be recommended; they are least sensitive to the stability errors. To detect changes in particle size, the high-end  $\tau$  are better suited.

## C. Noise and Digitization Errors

### 1. Aerosol Optical Depth

From the analysis of Section 4, the combined *ND* effect leads to the following typical rms and maximum errors of  $\tau$ :  $\sigma_{\tau 1ND} \sim 0.8 \times 10^{-2}$  and  $\sigma_{\tau 2ND} \sim 1.0 \times 10^{-2}$  (ranges of error,  $\Delta\tau_{1ND} \sim 6\sigma_{\tau 1ND} \sim 0.048$  and  $\Delta\tau_{2ND} \sim 6\sigma_{\tau 2ND} \sim 0.060$ ). The respective  $\eta_{\tau 1ND} \equiv \delta\tau/\Delta\tau_{1ND}$  and  $\eta_{\tau 2ND} \equiv \delta\tau/\Delta\tau_{2ND}$  are  $\sim 10$  and  $\sim 8$ , suggesting reliable separation of no more than approximately 8–10 classes of  $\tau$  in individual GAC pixel data.

### 2. Ångström Exponent

Of most practical interest is the case shown in Fig. 11c3, which corresponds to a combined *ND* effect from both channels 1 and 2. Analyses of Section 4, Eq. (9), and Figs. 9 and 11c3 suggest that the *ND* signal is distributed normally, with  $\sigma_{\alpha ND} = \sigma_{\alpha ND}^{(0)}/\tau_1 = 0.055/\tau_1$ , for an average geometry. The relative uncertainty is then  $\eta_{ND} = \sigma_{\alpha 0}/\sigma_{\alpha ND} \equiv \sigma_{\alpha 0}/\sigma_{\alpha ND}^{(0)}\tau_1 = (0.24 \pm 0.02)/0.055\tau_1 \approx (4.4 \pm 0.4)\tau_1$ , so  $\eta_{ND}$  increases linearly with  $\tau_1$ . In particular,  $\eta_{ND} = 1$  when  $\tau_{1ND}^{(0)} \approx 0.23 \pm 0.02$ . Over the whole 5°–25°S area, the vast majority of observations have

$\tau_1 < 2\tau_{1ND}^{(0)} (\sim 0.45 \pm 0.04)$ , for which no more than two classes of aerosol type can be reliably identified.

### 3. Improving the Relative Uncertainty

Averaging over  $n$  GAC pixels reduces  $\Delta\tau_{iND}$  and  $\Delta\alpha_{ND}$  by a factor of  $\sqrt{n}$ . Figure 14 gives an example of averaging AEROBS data in space and time ( $1^\circ \times 1^\circ \times 9$  days). Figure 14(a) is a histogram of the number of 8-km AEROBS cloud-free pixels within a box, which ranges typically from 1 to 20. (Note that AEROBS data are sampled GAC data and therefore are not representative of the full clear-sky AVHRR statistics.) Figures 14(b) and 14(c) show histograms of the averaged *ND* error in the retrieved  $\tau_1$  and  $\tau_2$  (cf. Figs. 9c3 and 9c4 for individual GAC pixels). The histograms of random errors in averaged data deviate from Gaussian, probably because of the substantial variability of the observation statistics from box to box, whereas their rms errors,  $\sigma_{\tau iND}$ , are reduced  $\sim 2.5$ -fold on average. Figure 14(d) shows a scattergram of  $\Delta\alpha_{ND}$  versus  $\tau_1$ :  $\Delta\alpha_{ND}$  increases toward low  $\tau$  [as in Fig. 10c3), but its magnitude is reduced by a factor of  $\sim 3.5$  from that of individual GAC pixels. (Note that the  $1/\tau_1$  trend in scatter is partially offset by the generally increased number of cloud free points within a box at low  $\tau$ . As a result,  $\sigma_{\alpha ND}$  is reduced more efficiently at low  $\tau$ ; hence the reduction rate is higher here than for the average  $\sigma_{\tau iND}$ ).

These results shed light on the expected reduction of the *ND* errors in the averaged data sets, such as the PATMOS<sup>30</sup> and the Goddard Institute for Space Studies (GISS) data sets used for the GACP.<sup>4</sup> In both, GAC pixels are averaged within  $\sim (1^\circ \times 1^\circ \times 1$  month) space–time boxes, yielding roughly a factor of  $(30/9) \sim 3.3$  *additional* increase in number of observations. Additionally, a factor of  $\sim 2.5$  increase comes from the use of original 4-km GAC pixels instead of the 8-km AEROBS pixels (in which averaging has already been performed over a few GAC pixels, whose number may vary from 1 to 4). This gives a factor of  $\sim 8.3 (=3.3 \times 2.5)$  increase in the number of observations. As a result, the *ND* errors will be further reduced by a factor of  $\sim 2.9 (= \sqrt{8.3})$ . When this reduction is combined with the factor of  $3.0 \pm 0.5$  reduction for data in Fig. 14, the averaging in PATMOS and GISS/GACP data thus reduces the *ND* errors by a factor of  $8.7 \pm 1.5$ . In particular,  $\sigma_{\tau iND} \sim (1.0 \pm 0.1) \times 10^{-3}$ , and the rms error in the Ångström exponent is approximated as  $\sigma_{\alpha ND} \sim (0.0065 \pm 0.0011)/\tau_1$ . The crossover point in  $\tau_1$ , where  $\eta \equiv \sigma_{\alpha 0}/\sigma_{\alpha ND} = 1$ , is reduced from  $\tau_1 \sim 0.25 \pm 0.03$  to  $\tau_1 \sim 0.03 \pm 0.01$ . Note, however, that this is an average estimate. The error in the averaged product depends strongly on the number of data points used and may have a regional or seasonal structure, e.g., as a result of cloud cover and sampling strategy. Great care, and individual analyses, are recommended in any case.

## 7. Conclusion

The sensitivity of aerosol optical depths from AVHRR channels 1 (0.63  $\mu\text{m}$ ) and 2 (0.83  $\mu\text{m}$ ),  $\tau_1$  and  $\tau_2$ , and

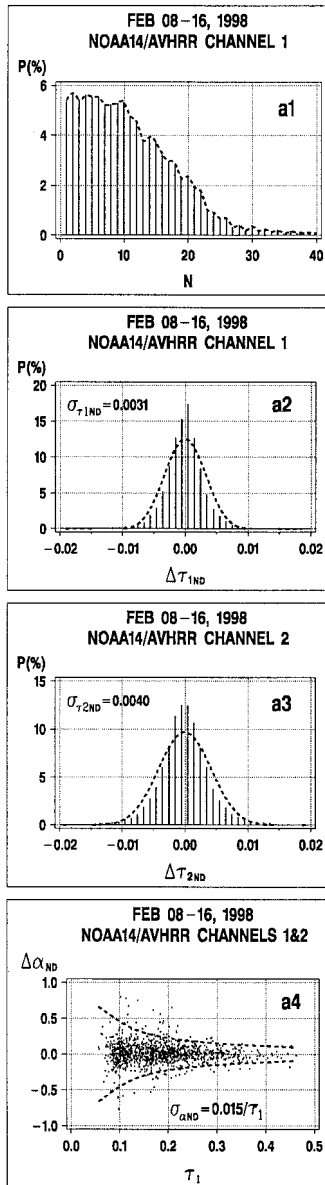


Fig. 14. Effect of ( $1^\circ \times 1^\circ$ ) averaging on the  $ND$  error in the AEROBS retrievals: a1, histogram of the number of clear sky pixels within ( $1^\circ \times 1^\circ$ ) boxes; a2, a3, histograms of averaged  $ND$  signals in channels 1 ( $\Delta\tau_{1ND}$ ; a2; cf. Fig. 9c3) and 2 ( $\Delta\tau_{2ND}$ ; a3; cf. Fig. 9c4); and a4, scattergram of averaged  $\Delta\alpha_{ND}$  versus  $\tau_1$  (cf. Fig. 10c3).

the Ångström exponent  $\alpha$  to the radiometric uncertainties (calibration and stability errors, radiometric noise, and digitization—the  $C$ ,  $S$ ,  $N$ , and  $D$  factors, respectively) have been examined empirically and theoretically. Empirical formulas, obtained for the NOAA-14 AVHRR, relate aerosol retrieval errors to the radiometric uncertainties. Theoretical analyses were made with a simplified radiative transfer equation to clarify the empirical findings and potentially to generalize them to be usable with the data from other sensors and satellites. The analytical sensitivity formulas provide a simple and convenient way to determine how a radiometric error propagates into

$\tau$  and  $\alpha$  retrievals, for a specific set of satellite sensor channels, under different aerosol and Sun and view geometry conditions. The parameters of the derived theoretical formulas may need fine tuning or adjustments to be used for quantitative error analyses with real data.

The calibration-induced uncertainties in aerosol optical depths are accurately predicted with Eqs. (5):  $\Delta\tau_{1C} = (0.37 + 0.71\tau_1)\epsilon_{1C}$  and  $\Delta\tau_{2C} = (0.16 + 0.74\tau_2)\epsilon_{2C}$ . For the best-case calibration errors ( $\epsilon_{1C} = \pm 0.05$ ,  $\epsilon_{2C} = \pm 0.07$ ),  $\Delta\tau_{1C}$  is  $\pm 0.019/0.037$  for  $\tau_1 = 0/0.5$  and  $\Delta\tau_{2C}$  is  $\pm 0.011/0.037$  for  $\tau_2 = 0/0.5$ . The corresponding uncertainties in the Ångström exponent are defined as  $\Delta\alpha_{1C} = +\Lambda \ln(1 + \Delta\tau_{1C}/\tau_1)$  and  $\Delta\alpha_{2C} = -\Lambda \ln(1 + \Delta\tau_{2C}/\tau_2)$ , where  $\Lambda$  is the spectral separation factor between the channels defined by Eq. (1) (for AVHRR,  $\Lambda \approx 3.63$ ). For practical applications, the logarithm permits expansion into Taylor's series, and the first (linear) term accurately approximates the nonlinear logarithmic function:  $\Delta\alpha_{1C} \sim +\Lambda \times \Delta\tau_{1C}/\tau_1$  and  $\Delta\alpha_{2C} \sim -\Lambda \times \Delta\tau_{2C}/\tau_2$  (cf. Ref. 11). For typical open-ocean conditions ( $\tau \sim 0.15$ ),  $\Delta\alpha_C$  is  $\pm 0.53 \mp 0.43$ , which is comparable to the range of variability of the Ångström exponent itself ( $\pm 0.65$ , according to the analysis of Ignatov and Stowe<sup>32</sup>). To check whether systematic error is present in  $\alpha$  retrievals it is useful to plot the retrieved  $\alpha$  versus  $\tau$ . Adjustment to the calibration can be made based on anchoring the retrieved  $\alpha$  to ground-based sunphotometer measurements or to climatology. Monitoring or adjusting calibration stability or both, based on global conglomerate  $\tau$  or  $\alpha$ , may be practical because the angular signal, which is present in radiances, is removed when the radiances are converted to the retrieved aerosol parameters, which are thus expected to be more sensitive to the calibration uncertainties. (The Sun-view geometry trends in the calibration-induced errors,  $\Delta\tau_{iC}$  and  $\Delta\alpha_{iC}$ , were specially analyzed and shown to be negligible).

Unlike the systematic effect of the calibration-induced error on aerosol retrievals, radiometric noise ( $N$ ) and digitization ( $D$ ) introduce no bias in the retrieved  $\tau$  and  $\alpha$  but contribute to random errors. The  $D$  signal is distributed uniformly, whereas the  $N$  and the combined  $ND$  signals are distributed normally. According to Eqs. (16), rms error in  $\tau_i$  and  $\sigma_{\tau iX}$  depends on view geometry as  $\sigma_{\tau iX} = (4\mu_V/p_i^A)\sigma_{AiX}$ , where  $\sigma_{AiX}$  is the rms deviation of the albedo in channel  $i$  that is due to noise ( $X = N$ ), to digitization ( $X = D$ ), or to their combination ( $X = ND$ ). According to Eqs. (9), the rms error in  $\alpha$ ,  $\sigma_{\alpha iX}$ , is calculated as  $\sigma_{\alpha iX} \sim \Lambda\sigma_{\tau iX}/\tau_i$ . The combined  $ND$  signals in the albedos,  $\tau$  and  $\alpha$ , are calculated from the respective  $N$  and  $D$  components in a rms sense as  $\sigma_{AiND} = (\sigma_{AiN}^2 + \sigma_{AiD}^2)^{1/2}$ ,  $\sigma_{\tau iND} = (\sigma_{\tau iN}^2 + \sigma_{\tau iD}^2)^{1/2}$ , and  $\sigma_{\alpha iND} = (\sigma_{\alpha iN}^2 + \sigma_{\alpha iD}^2)^{1/2}$ . Note that the  $N$  and  $D$  contributions to the  $ND$  signal are comparable for all variables. We calculated a combined effect on the Ångström exponent from the two channels by summing the contributions of the individual channels in a rms sense:  $\sigma_{\alpha X} = (\sigma_{\alpha 1X}^2 + \sigma_{\alpha 2X}^2)^{1/2}$ . Note that



channel 2 contributes  $\sim 1.5$  times more than channel 1 to the rms error in the Ångström exponent. All components of  $\alpha$  error can be approximated as  $\sigma_{\alpha iX} \sim \sigma_{\alpha iX}^{(0)}/\tau_1$ . When both  $N$  and  $D$  effects are taken into account in both channels, then  $\sigma_{\alpha ND}^{(0)} = 0.055$  for individual GAC pixels. Averaging data in space and time reduces the random errors. It may, however, make them non-Gaussian and nonuniform in space and time. Care must be used to ensure that sufficient numbers of points are available in each grid cell.

Retrieval of the Ångström exponent (and any size parameter, for that matter) is, generally, a bigger challenge than the retrieval of aerosol optical depth. This observation is true not only for satellite observations, such as from AVHRR.<sup>41,42</sup> It is also in a broad agreement with the results of other authors obtained with sunphotometry, which is but a simpler case of satellite retrievals. Ångström<sup>43,44</sup> explicitly articulated “the need of greater accuracy in the radiation measurements, on which all methods for determining the turbidity parameters must be based,” especially the differential aerosol size parameter. For any sensor, radiometrically induced errors in the retrieved size parameters increase toward low  $\tau$ , whereas the relative uncertainty,  $\eta$ , decreases. For individual AVHRR GAC pixels, a crossover point where  $\eta_{ND} = 1$  is  $\tau_{1ND}^{(0)} \sim (0.25 \pm 0.02)$ . For  $\tau_1 < \tau_{1ND}^{(0)}$ , the  $\alpha$  signal is composed mostly of the  $ND$  errors in the two channels and carries little useful information on the particles’ size. As  $\tau$  increases, the aerosol contribution to the estimated  $\alpha$  increases, too, but the noise is still present. For a two-channel radiometer, such as the NOAA/AVHRR or the Visible and Infrared Scanner (VIRS) on board the Tropical Rainfall Measuring Mission (TRMM) Satellite, threshold  $\tau_1^{(0)}$  is defined mainly by two factors: errors in individual channel retrievals (which can be reduced by space–time averaging) and the spectral separation of the channels,  $\Delta$ , which amplifies all individual errors and uncertainties in the channels. Aerosol retrievals from the advanced sensors are expected to do a better job of aerosol retrieval, owing to the superior performance of their individual channels, their increased number, and better spectral coverage.<sup>45</sup> All these factors contribute to the improved accuracy of the derived size parameter, especially at low aerosols, by lowering the parameter’s threshold of usefulness.

John Sapper’s contribution to the development on a mainframe of the AEROBS software used for this study is greatly appreciated. Thanks are due to Lee Dantzler (Manager of the NOAA Ocean Remote Sensing Program, NOAA/NESDIS) and Bruce Wielicki and Bruce Barkstrom (NASA TRMM/Clouds and the Earth’s Radiant Energy System (CERES) program, contract L-90987C), for support and encouragement; Larry Stowe NOAA/NESDIS, retired, Nagaraja Rao (NOAA/NESDIS, deceased), and Ross Mitchell (Commonwealth Scientific and Industrial Research Organisation, Australia) for helpful discussions; Karen Michels (NOAA), Nick Nalli (NOAA/NESDIS)

and Lucille Halberstadt (Optical Society of America) for editorial help; and two reviewers for careful review of the paper and suggested changes to it (in particular, use of the term “relative uncertainty”).

## References

1. L. Stowe, A. Ignatov, and R. Singh, “Development, validation, and potential enhancements to the second-generation operational aerosol product at NOAA/NESDIS,” *J. Geophys. Res.* **102**, 16,923–16,934 (1997).
2. A. Ignatov and L. Stowe, “Aerosol retrievals from individual AVHRR channels. I. Retrieval algorithm, and transition from Davé to 6S radiative transfer model,” *J. Atmos. Sci.* (to be published).
3. E. Vermote, D. Tanre, J. L. Deuze, M. Herman, and J. J. Morcrette, “Second simulation of the satellite signal in the solar spectrum, ‘6S’: an overview,” *IEEE Trans. Geosci. Remote Sens.* **35**, 675–686 (1997).
4. M. I. Mishchenko, I. V. Geogdzhayev, B. Cairns, W. B. Rossow, and A. Lacis, “Aerosol retrievals over the oceans by use of channels 1 and 2 AVHRR data: sensitivity analysis and preliminary results,” *Appl. Opt.* **38**, 7325–7341 (1999).
5. H. R. Gordon, “Reduction of error introduced in the processing of coastal zone color scanner type imagery resulting from sensor calibration and solar irradiance uncertainty,” *Appl. Opt.* **20**, 207–210 (1981).
6. H. R. Gordon, “Radiometric considerations for ocean color remote sensors,” *Appl. Opt.* **29**, 3228–3236 (1990).
7. P. Durkee, F. Pfeil, E. Frost, and E. Shima, “Global analysis of aerosol particle characteristics,” *Atmos. Environ. A* **25**, 2457–2471 (1991).
8. R. Wagener, S. Nemesure, and S. E. Schwartz, “Aerosol optical depth over oceans: high space- and time-resolution retrieval and error budget from satellite radiometry,” *J. Atmos. Ocean. Technol.* **14**, 577–590 (1997).
9. A. Higurashi and T. Nakajima, “Development of a two-channel aerosol retrieval algorithm on a global scale using NOAA/AVHRR,” *J. Atmos. Sci.* **56**, 924–941 (1999).
10. A. Ignatov and L. Stowe, “Physical basis, premises, and self-consistency checks of aerosol retrievals from TRMM VIRS,” *J. Appl. Meteorol.* **39**, 2259–2277 (2000).
11. A. Ignatov, L. Stowe, and R. Singh, “Sensitivity study of the Ångström exponent derived from AVHRR over the oceans,” *Adv. Space Res.* **21**, 439–442 (1998).
12. N. Che and J. Price, “Survey of radiometric calibration results and methods for visible and near infrared channels of NOAA-7, -9, and -11 AVHRRs,” *Remote Sens. Environ.* **41**, 19–27 (1992).
13. P. Abel, B. Guenther, R. Galimore, and J. Cooper, “Calibration results for NOAA-11 AVHRR channels 1 and 2 from coherent path aircraft observations,” *J. Atmos. Ocean. Technol.* **10**, 493–508 (1993).
14. N. Rao and J. Chen, “Post-launch calibration of the visible and near-infrared channels of the Advanced Very High Resolution Radiometer on the NOAA-14 spacecraft,” *Int. J. Remote Sens.* **17**, 2743–2747 (1996).
15. K. Kidwell, *NOAA Polar Orbiter Data User’s Guide* (U.S. Government Printing Office, Washington, D.C., 1995, 630–673).
16. F. Staylor, “Degradation rates of the AVHRR visible channel for the NOAA 6, 7, and 9 spacecraft,” *J. Atmos. Ocean. Technol.* **7**, 411–423 (1990).
17. P. Teillet, P. Santer, Y. Ding, R. Santer, R. Jackson, and M. Moran, “Three methods for the absolute calibration of the NOAA AVHRR sensors in-flight,” *Remote Sens. Environ.* **31**, 105–120 (1990).
18. R. Mitchell, D. O’Brien, and B. Forgan, “Calibration of the



- AVHRR shortwave channels using split pass imagery. I. Pilot study," *Remote Sens. Environ.* **40**, 57–65 (1992).
19. R. Mitchell, D. O'Brien, and B. Forgan, "Calibration of the AVHRR shortwave channels. II. Application to NOAA-11 during early 1991," *Remote Sens. Environ.* **55**, 139–152 (1996).
  20. Y. Kaufman and B. Holben, "Calibration of the AVHRR visible and near-IR bands by atmospheric scattering, ocean glint, and desert reflection," *Int. J. Remote Sens.* **14**, 21–52 (1993).
  21. J. Cihlar and P. Teillet, "Forward piecewise linear calibration model for quasi-real time processing of AVHRR data," *Can. J. Remote Sens.* **21**, 22–27 (1995).
  22. N. Rao and J. Chen, "Inter-satellite calibration linkages for the visible and near-infrared channels of the Advanced Very High Resolution Radiometer on the NOAA-7, -9, and -11 spacecraft," *Int. J. Remote Sens.* **16**, 1931–1942 (1995).
  23. E. Vermote and Y. Kaufman, "Absolute calibration of the AVHRR visible and near-IR channels using ocean and cloud views," *Int. J. Remote Sens.* **16**, 2317–2340 (1995).
  24. C. Brest, W. Rossow, and M. Roiter, "Update of radiance calibration for ISCCP," *J. Atmos. Ocean. Technol.* **14**, 1091–1109.
  25. N. Loeb, "In-flight calibration of NOAA AVHRR visible and near-IR bands over Greenland and Antarctica," *Int. J. Remote Sens.* **18**, 477–490 (1997).
  26. N. Rao and J. Chen, "Revised post-launch calibration of the visible and near-infrared channels of the Advanced Very High Resolution Radiometer on the NOAA-14 spacecraft," *Int. J. Remote Sens.* **20**, 3485–3491 (1999).
  27. H. Neckel and D. Labs, "The solar radiation between 3300 and 12500 Å," *Solar Phys.* **90**, 205–208 (1984).
  28. R. Mitchell, "In-flight characteristics of the space count of NOAA AVHRR channels 1 and 2," *CSIRO Res. Rep.* **52**, 1–24 (2001).
  29. R. Mitchell, "Pre-flight calibration anomaly in the NOAA14 AVHRR channels 1 and 2," *Remote Sens. Environ.* **56**, 141–147 (1996).
  30. L. Stowe, H. Jacobowitz, G. Ohring, K. Knapp, and N. Nalli, "The Advanced Very High Resolution Radiometer Pathfinder Atmosphere (PATMOS) dataset: initial analyses and evaluation," submitted to *J. Clim.*
  31. P. McClain, "Global SST and cloud clearing for aerosol optical depth estimates," *Int. J. Remote Sens.* **10**, 763–769 (1989).
  32. A. Ignatov and L. Stowe, "Aerosol retrievals from individual AVHRR channels. II. Quality control, probability distribution functions, and consistency checks of retrievals," *J. Atm. Sci.* (to be published).
  33. M. Viollier, D. Tanre, and P. Y. Deschamps, "An algorithm for remote sensing of water color from space," *Boundary-Layer Meteorol.* **18**, 247–267 (1980).
  34. H. Gordon and P. Morel, *Remote Assessment of Ocean Color for Interpretation of Satellite Visible Imagery: a Review* (Springer-Verlag, New York, 1983).
  35. E. R. Westwater and O. N. Strand, "Statistical information content of radiation measurements used in indirect sensing," *J. Atmos. Sci.* **25**, 750–758 (1968).
  36. C. D. Rogers, "Retrieval of atmospheric temperature and composition from remote measurements of thermal radiation," *Rev. Geophys. Space Phys.* **14**, 609–624 (1976).
  37. T. Aoki, "On the information content of the satellite measured infrared radiation in the atmospheric window region," *J. Meteorol. Soc. Jpn.* **56**, 508–515 (1979).
  38. N. O'Neill, A. Ignatov, B. Holben, and T. Eck, "The log-normal distribution as a reference for reporting aerosol optical depth statistics: empirical tests using multi-year, multi-site AERONET sun-photometer data," *Geophys. Res. Lett.* **27**, 3333–3336 (2000).
  39. U.S. Navy, "Marine Climatic Atlas of the World," CD-ROM, Version 1.0 (Naval Oceanography Command Detachment, Asheville, N.C., 1992).
  40. R. H. Evans and H. Gordon, "Coastal zone color scanner system calibration: a retrospective examination," *J. Geophys. Res.* **99**, 7293–7307 (1994).
  41. Y. Kaufman, R. Fraser, and R. Ferrare, "Satellite measurements of large-scale air pollution: methods," *J. Geophys. Res.* **95**, 9895–9909 (1990).
  42. Y. Kaufman, "Aerosol optical thickness and atmospheric path radiance," *J. Geophys. Res.* **98**, 2677–2692 (1993).
  43. A. Ångström, "Techniques of determining the turbidity of the atmosphere," *Tellus* **13**, 214–223 (1961).
  44. A. Ångström, "The parameters of atmospheric turbidity," *Tellus* **16**, 214–223 (1964).
  45. Y. Kaufman, D. Tanre, H. Gordon, T. Nakajima, J. Lenoble, R. Frouin, H. Grassl, B. M. Herman, M. D. King, and P. M. Teillet, "Passive remote sensing of tropospheric aerosol and atmospheric correction for aerosol effect," *J. Geophys. Res.* **102**, 16,815–16,830 (1997).